ENHANCING THE RESOLUTION OF MULTIMODE FIBER BASED SPECTROMETERS

A THESIS SUBMITTED TO
THE GRADUATE SCHOOL OF NATURAL AND APPLIED SCIENCES
OF
MIDDLE EAST TECHNICAL UNIVERSITY

BY

SIDDIK SÜLEYMAN KAHRAMAN

IN PARTIAL FULFILLMENT OF THE REQUIREMENTS
FOR
THE DEGREE OF MASTER OF SCIENCE
IN
PHYSICS

SEPTEMBER 2021

Approval of the thesis:

ENHANCING THE RESOLUTION OF MULTIMODE FIBER BASED SPECTROMETERS

submitted by **SIDDIK SÜLEYMAN KAHRAMAN** in partial fulfillment of the requirements for the degree of **Master of Science in Physics Department, Middle East Technical University** by,

Prof. Dr. Halil Kalıpçılar
Dean, Graduate School of **Natural and Applied Sciences** _____

Prof. Dr. Seçkin Kürkcüoğlu
Head of Department, **Physics** _____

Assoc. Prof. Dr. Emre Yüce
Supervisor, **Physics, METU** _____

Examining Committee Members:

Prof. Dr. Hakan Altan
Physics, METU _____

Assoc. Prof. Dr. Emre Yüce
Physics, METU _____

Prof. Dr. İsa Navruz
Electrical and Electronics Engineering, Ankara University _____

Date: 06.09.2021

I hereby declare that all information in this document has been obtained and presented in accordance with academic rules and ethical conduct. I also declare that, as required by these rules and conduct, I have fully cited and referenced all material and results that are not original to this work.

Name, Surname: Sıddık Süleyman Kahraman

Signature :

ABSTRACT

ENHANCING THE RESOLUTION OF MULTIMODE FIBER BASED SPECTROMETERS

Kahraman, Sıddık Süleyman
M.S., Department of Physics
Supervisor: Assoc. Prof. Dr. Emre Yüce

September 2021, 70 pages

Speckle-based spectrometers are shown to reach resolving powers that exceed the state-of-the-art grating spectrometers. These spectrometers offer high-resolution by relying on a complex spectral to spatial mapping. Multimode fibers (MMFs) reduce losses that occur from scattering of light and can also provide spectral to spatial mapping. The resolution of a MMF based spectrometer can be increased using longer fibers that in return makes them susceptible to environmental changes. This study introduces techniques based on wavefront shaping (WFS) to enhance the spectral resolution without changing the fiber parameters. The methods introduced here manage to enhance the spectral resolution of a MMF based spectrometer by nearly twice and demonstrate down to 5 pm resolution reaching a record resolution in the telecom range.

Keywords: Multimode fiber, spectrometer, wavefront shaping

ÖZ

ÇOK MODLU FİBER TABANLI SPEKTROMETRELERİN ÇÖZÜNÜRLÜĞÜNÜN ARTIRILMASI

Kahraman, Sıddık Süleyman
Yüksek Lisans, Fizik Bölümü
Tez Yöneticisi: Doç. Dr. Emre Yüce

Eylül 2021 , 70 sayfa

Saçılım tabanlı spektrometreler, son teknoloji kırınım ızgarası temelli spektrometrelerin sahip olduğu çözme gücüne erişebilmektedirler. Bu tip spektrometrelerin sunduğu yüksek çözünürlükler karmaşık spektral-uzaysal eşleştirmeye dayanmaktadır. Çok modlu fiberler ışığın saçılımından dolayı oluşan kayıpları azaltırlar ve spektral bilgiyi uzaysal konuma eşleştirmede de kullanılabilirler. Çok modlu fiber tabanlı spektrometrelerin çözünürlükleri daha uzun fiberler kullanılarak artırılabilir fakat bu durum onları çevresel değişimlere karşı daha duyarlı hale getirir. Bu tez çalışması fiber parametrelerini değiştirmeden spektral çözünürlüğü artırmaya yarayan dalgaönü şekillendirme tabanlı yeni teknikler sunmaktadır. Sunulan metotlar çok modlu fiber tabanlı bir spektrometrenin spektral çözünürlüğünü yaklaşık iki kat artırıp 5 pm değerine kadar gelişerek telekom dalgaboylarında rekor seviyede çözünürlük sunmaktadır.

Anahtar Kelimeler: Çok modlu fiber, spektrometre, dalga önü şekillendirme

To the authenticity and inadequacy of science

ACKNOWLEDGMENTS

First and foremost, I would like to acknowledge my advisor Emre Yüce. I am grateful for his relentless support and brilliant supervision. His teachings will always be useful throughout my academic and personal life. I am greatly indebted to my dear friend and colleague Şahin Kürekci for working with me day and night. I appreciate my friends who have been there for me in my desperate need, especially Alim Yolalmaz. I hope there is a way for me to reciprocate all my fellow lab members who helped me along the way. Last but not least, I thank my family for their unconditional support.

I would like to acknowledge the financial support provided by TUBITAK under program no 2210-E. This study has also been funded by TUBITAK grant no 118M199 and 118E995.

TABLE OF CONTENTS

LIST OF TABLES

TABLES

LIST OF FIGURES

FIGURES

LIST OF ABBREVIATIONS

2D	2 Dimensional
3D	3 Dimensional
MMF	Multimode Fiber
WFS	Wavefront Shaping
SLM	Spatial Light Modulator
LP	Linearly Polarized
TM	Transmission Matrix
CW	Continuous Wave
FWHM	Full Width at Half Maximum
FWHP	Full Width at Half Prominence
MSE	Mean Squared Error
RMSE	Root Mean Squared Error

CHAPTER 1

INTRODUCTION

1.1 Spectral Analysis

Most common spectrometers utilize a diffraction grating which maps each wavelength to a different coordinate in space. A sensor placed on the range of coordinates can measure the intensity at of the incoming light. Due to the one-to-one spectral-to-spatial mapping, each sensor measures the intensity of a different wavelength [1]. Fig. 1.1 shows illustrations of prism based (a) and grating based (b) conventional spectrometers. Each wavelength is oriented at a separate direction, and multiple sensors are placed at different positions after some distance.

While these spectrometers have a wide range of bandwidth, the spectral resolution is often too low. The limiting factor is usually the physical size of the spectrometer. In order to overcome this issue, one of the alternatives is to create a more complicated spectral-to-spatial mapping. Various scattering media, such as a diffuser, can be used for this purpose. However, the downside of spectrometers using scattering media is the energy loss. A large portion of the incoming beam do not reach the sensors. Multimode fiber based spectrometers solve this issue since the energy loss is very low and a complex spectral-to-spatial mapping can still be achieved [2].

1.2 Multimode Fiber Based Spectrometers

Scattering medium-based spectrometers can be compact and provide much higher spectral resolution than conventional spectrometers [3–6]. However, scattering from rough surfaces introduce high loss. Instead, multi-mode fiber (MMF) based spec-

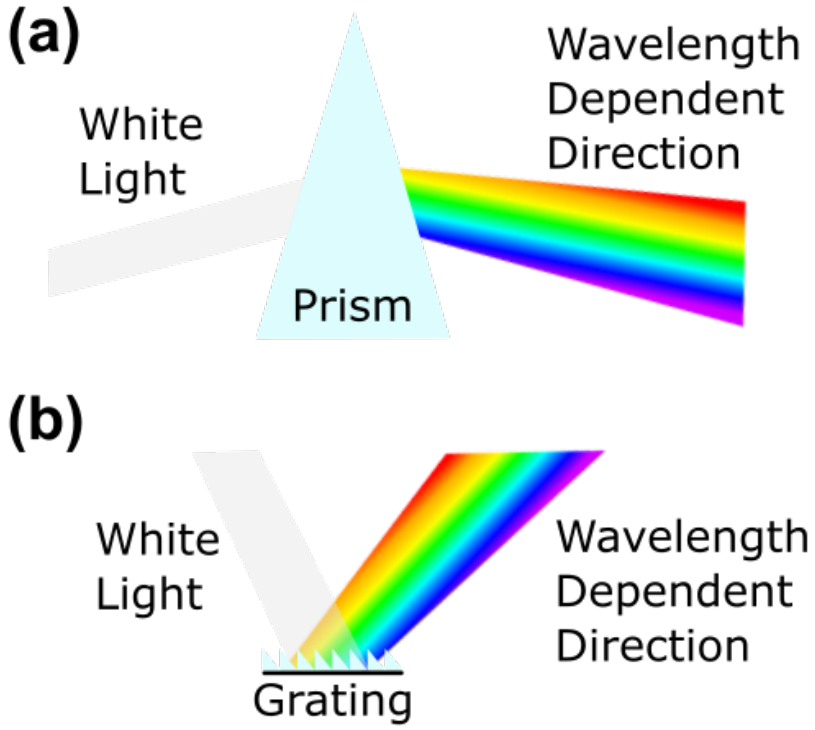

Figure 1.1: **(a)** An illustration of a prism based conventional spectrometer. **(b)** An illustration of a grating based conventional spectrometer.

trometers, and equivalently multi-mode waveguides offer high-resolution, low loss, and compact solutions for spectral reconstruction [7–16].

When a light beam is coupled into a multimode fiber, the output of the fiber is usually a speckle pattern as illustrated in Fig. 1.2. MMF's have different propagating modes of electromagnetic waves which travel at slightly different speeds along the axis of the fiber. This difference creates a time delay at the end of the fiber and all the modes interfere with seemingly random phases. The total interference creates these speckle patterns which allow complex spectral-to-spatial mapping [17].

First discovered in 1980's [18], MMF spectrometers have been studied intensively in the literature [2, 9–11, 15, 16]. The sensitivity of the propagation constants and thus the interference on the incoming wavelength assures that these spectrometers have very high spectral resolution. While depending on several factors, the spectral resolution is proportional to the length of the fiber [9]. Since the energy loss of

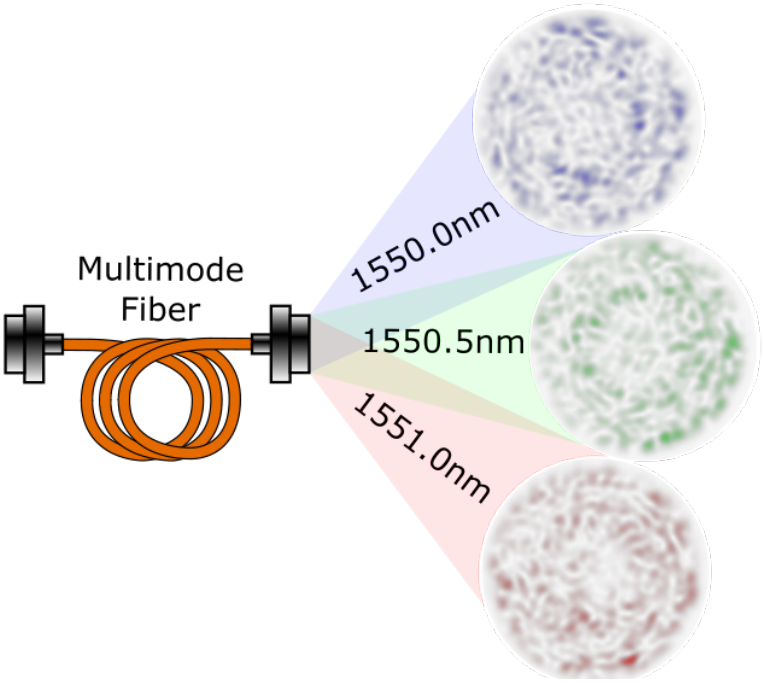

Figure 1.2: An illustration of the output speckle patterns created by a MMF at different wavelengths.

commercially available fibers is very low, it is convenient to simply increase the fiber length for higher resolution. However, the output speckle patterns are very susceptible to environmental factors such as temperature, humidity, and acoustic vibrations [2, 19]. These factors are enhanced when the fiber is longer. Therefore, it is desirable to increase the spectral resolution without increasing the fiber length.

Here, we report techniques using wavefront shaping (WFS) to increase the spectral resolution of MMF-based spectrometers. While the speckle phenomena have been known for a long time [19], only recent improvements of WFS technologies allowed a variety of applications [20–23]. Some of these applications include strong control over speckle patterns with focusing and imaging through strongly scattering media like MMF's using feedback based [24–28], transmission matrix based [27, 29–38], and deep learning based [39–44] techniques. Furthermore, multi-core MMF's have been used for hyperspectral imaging exploiting the fact that the spectrum can be reconstructed from a single speckle pattern [45, 46]. In these applications the structural properties of scattering media is characterized using SLM's [47] but MMF-based spectrometers are yet to utilize WFS techniques. Similar to techniques used in mi-

croscopy studies such as structured illumination microscopy [48] the additional degree of spatial control provided by SLMs can be utilized to gain additional control in the frequency domain.

1.3 Contributions and Novelties

The recent developments regarding Spatial Light Modulators are promising for spectrometer design as well as many other fields. In this thesis, we use an SLM to shape the wavefront of the beam coupled into the fiber. This changes the energy distribution among the fiber modes as well as the output speckle patterns. The output speckle patterns are then processed to create a spectrometer that has a higher spectral resolution. Our techniques allow the use of a shorter MMF without any compromise in the bandwidth at an increased spectral resolution. We predict that the methodology that we introduce here will pave the way for increased spectral resolution using even more advanced processing methods.

Our contribution is in obtaining MMF spectrometers with record level high spectral resolutions. Our novelty is in modifying the spectral behaviour through spatial modulation of a spatial-spectral coupled optical system.

1.4 The Outline of the Thesis

In this thesis, MMF physics will be explained and illustrated in the Theory and Simulation chapter. The experimental setups used will be explained in the Experimental Setups chapter. Then, some of the methods attempted by the author will be listed and explained, and their results will be shared in Methods and Results chapter. Final results, and potential future work will be discussed in the Conclusion chapter.

CHAPTER 2

THEORY AND SIMULATION

2.1 Physics of Multimode Fibers

The fibers used in this study are all cylindrical step-index fibers. The Maxwell's equations can be simplified into Eq. 2.1 and 2.2 in homogeneous and lossless dielectric [17]. These assumptions can be made for the fibers used here. In homogeneous and lossless dielectric media [17], the Maxwell's equations can be simplified into

$$\nabla \times \mathbf{E} = -\mu \frac{\partial \mathbf{H}}{\partial t}, \tag{2.1}$$

$$\nabla \times \mathbf{H} = \varepsilon \frac{\partial \mathbf{E}}{\partial t}. \tag{2.2}$$

These assumptions can be made for the cylindrical step-index fibers used in this study. At this point, the direction of the fields should be chosen. Transverse electric, transverse magnetic and hybrid modes are the fundamental alternatives which result in different solutions. There is a different convention that encapsulates all solutions called Linearly Polarized (LP) modes which work under the weak guiding assumption, $n_{core} - n_{clad} << n_{core}$ [17]. LP modes are superposition of the different alternative solutions and have fields with a fixed direction and polarization. Generating LP modes in the experiments is practical because a simple laser or a polarizer can ensure a linear polarization. Assuming the solutions of interest are linearly polarized electromagnetic waves propagating in the $+\hat{z}$ direction, they can be written in the

form

$$\mathbf{E} = E\left(r,\theta\right)\ e^{i(\omega t-\beta z)}, \tag{2.3}$$

$$\mathbf{H} = H\left(r,\theta\right)\ e^{i(\omega t-\beta z)}, \tag{2.4}$$

where, β is the wavevector and ω is the laser frequency. Since the electric and magnetic field solutions are similar, it is sufficient to solve only the electric field. Using all the previous equations, the differential equation for the electric field can be reduced to the Helmholtz Equation

$$\left(\frac{\partial^2}{\partial r^2}+\frac{1}{r}\frac{\partial}{\partial r}+\frac{1}{r^2}\frac{\partial^2}{\partial\theta^2}+k_0^2n^2\right)E\left(r,\theta\right)=\beta^2E\left(r,\theta\right). \tag{2.5}$$

Using separation of variables, $E\left(r,\theta\right)=E_r\left(r\right)E_\theta(\theta)$, the solutions can be separated into radial and azimuthal parts. The azimuthal solution would be

$$E_\theta\left(\theta\right)=\cos\left(m\theta+\phi\right), \tag{2.6}$$

where, m is a non-negative integer due to azimuthal boundary conditions. The radial solution can be written as

$$E_{r,mp}(r)=\begin{cases}J_m\left(U\frac{r}{a}\right), & \text{if } r<a,\\ K_m\left(W\frac{r}{a}\right), & \text{otherwise.}\end{cases} \tag{2.7}$$

Here, U and W, called normalized wavenumbers, are defined as

$$U=a\sqrt{k_0^2n_{core}^2-\beta^2}, \tag{2.8}$$

$$W=a\sqrt{\beta^2-k_0^2n_{clad}^2}. \tag{2.9}$$

The exact solutions to Eq. 2.7 are determined from the boundary conditions at $r = a$. These boundary conditions can be written as

$$E_r\left(a^+\right) = E_r\left(a^-\right), \tag{2.10}$$

$$\frac{\partial E_r\left(a^+\right)}{\partial r} = \frac{\partial E_r\left(a^-\right)}{\partial r}. \tag{2.11}$$

When boundary conditions are applied to Eq. 2.7, the characteristic equation can be obtained,

$$C_m\left(\beta\right) = U\frac{J_{m+1}\left(U\right)}{J_m\left(U\right)} - W\frac{K_{m+1}\left(W\right)}{K_m\left(W\right)} = 0. \tag{2.12}$$

This characteristic equation cannot be solved analytically. In order to further analyze the system, it is much more convenient to insert numerical values for the relevant parameters and solve the characteristic equation through numerical analysis. The solutions to the characteristic equation can be represented as β_{mp} where p is a positive integer. Using Eq. 2.6 to Eq. 2.9, the solution involving β_{mp} will be

$$E_{mp}(r,\theta) = \begin{cases} J_m\left(r\sqrt{k_0^2 n_{core}^2 - \beta_{mp}^2}\right)\cos\left(m\theta+\phi\right), & \text{if } r < a, \\ K_m\left(r\sqrt{\beta_{mp}^2 - k_0^2 n_{clad}^2}\right)\cos\left(m\theta+\phi\right), & \text{otherwise.} \end{cases} \tag{2.13}$$

The final solution in Eq. 2.3 involving the z-dependence can be rewritten as

$$\mathbf{E}_{mp} = \begin{cases} J_m\left(r\sqrt{k_0^2 n_{core}^2 - \beta_{mp}^2}\right)\cos\left(m\theta+\phi\right)e^{i(\omega t-\beta z)}, & \text{if } r < a, \\ K_m\left(r\sqrt{\beta_{mp}^2 - k_0^2 n_{clad}^2}\right)\cos\left(m\theta+\phi\right)e^{i(\omega t-\beta z)}, & \text{otherwise.} \end{cases} \tag{2.14}$$

The actual solution is the summation of all the particular solutions. The solutions can also be separated as even and odd. Thus, the complete should be written as

$$\mathbf{E}_{total} = \mathbf{E}_{even} + \mathbf{E}_{odd} \tag{2.15}$$

where, $\mathbf{E}_{even}$ and $\mathbf{E}_{odd}$ are

$$\mathbf{E}_{\text{even}} = \begin{cases} \sum_{mp} c_{mp}^{\text{even}} J_m \left(r\sqrt{k_0^2 n_{core}^2 - \beta_{mp}^2} \right) \cos(m\theta) e^{i(\omega t - \beta_{mp} z)}, & \text{if } r < a \\ \sum_{mp} c_{mp}^{\text{even}} K_m \left(r\sqrt{\beta_{mp}^2 - k_0^2 n_{clad}^2} \right) \cos(m\theta) e^{i(\omega t - \beta_{mp} z)}, & \text{if } r \geq a \end{cases} \tag{2.16}$$

$$\mathbf{E}_{\text{odd}} = \begin{cases} \sum_{mp} c_{mp}^{\text{odd}} J_m \left(r\sqrt{k_0^2 n_{core}^2 - \beta_{mp}^2} \right) \sin(m\theta) e^{i(\omega t - \beta_{mp} z)}, & \text{if } r < a \\ \sum_{mp} c_{mp}^{\text{odd}} K_m \left(r\sqrt{\beta_{mp}^2 - k_0^2 n_{clad}^2} \right) \sin(m\theta) e^{i(\omega t - \beta_{mp} z)}, & \text{if } r \geq a \end{cases} \tag{2.17}$$

Here, the coefficient of each LP mode, c_{mp}, is represented by two different variables for even and odd modes. These coefficients are related to the energy transferred in a particular mode which is proportional to $|c_{mp}|^2$.

In a realistic scenario, the mode coefficients at the input and the output would be different from each other. In an experimental environment, the MMF will not be as ideal as it is in the theoretical approach, both in terms of geometry and material imperfections. Therefore, the energies transferred in different modes will couple into each other. Thus, it is necessary to define a different set of coefficients representing the energy distribution at the output. Let $\mathbf{c}_{\text{in}}$ be a vector representing all the c_{mp}^{odd} and c_{mp}^{even} values at the input. Similarly, let the vector $\mathbf{c}_{\text{out}}$ represent all the mode coefficients at the fiber output. Depending on the specific position, time, temperature, humidity, material imperfections etc. there will be a matrix which will give the relation between $\mathbf{c}_{\text{in}}$ and $\mathbf{c}_{\text{in}}$. This matrix, $\mathbf{T}$, is called the mode-to-mode transmission matrix (TM). Using this TM, the output coefficients can be calculated from the input coefficients as

$$\mathbf{c}_{\text{out}} = \mathbf{T}\mathbf{c}_{\text{in}} \tag{2.18}$$

where the size of $\mathbf{c}_{\text{in}}$ and $\mathbf{c}_{\text{out}}$ are N_{mode}x1 and the size of $\mathbf{T}$ is N_{mode}xN_{mode}. This is true in the linear relationship case. In simulations, this TM can be set to practically any value. However, in experiments, it should be calculated beforehand in order to utilize it.

2.2 Numerical Simulation of a Multimode Fiber

The simulations are consulted when the analytical approaches become inconvenient such as for the characteristic equation. In order to find all the solutions, the β_{mp} values for which $C_m(\beta)$ is very close to 0 should be found. Numerical analysis, here, is straightforward, $C_m(\beta)$ is calculated for the range of possible β values for each m value. The indices at which the equation converts from a positive value to a negative value contains the solution. Unfortunately, the precision of the solutions will only be as fine as the step size. However, the precision is improved by inserting the range and the characteristic equation into a built-in MATLAB function called `fzero` that uses an optimization algorithm [49]. Fig. 2.1 illustrates an example of such a procedure. For $a = 7.5\mu$m, $a/\lambda = 15$ and $m = 0$, solutions with 4 different β values are found. The MATLAB codes written by [49,50] which find the LP modes and their spatial distributions are useful for the results in the first two figures. All other results involving LP mode summations, z dependence, wavelength dependence, transmission matrix etc. require further implementations as developed here.

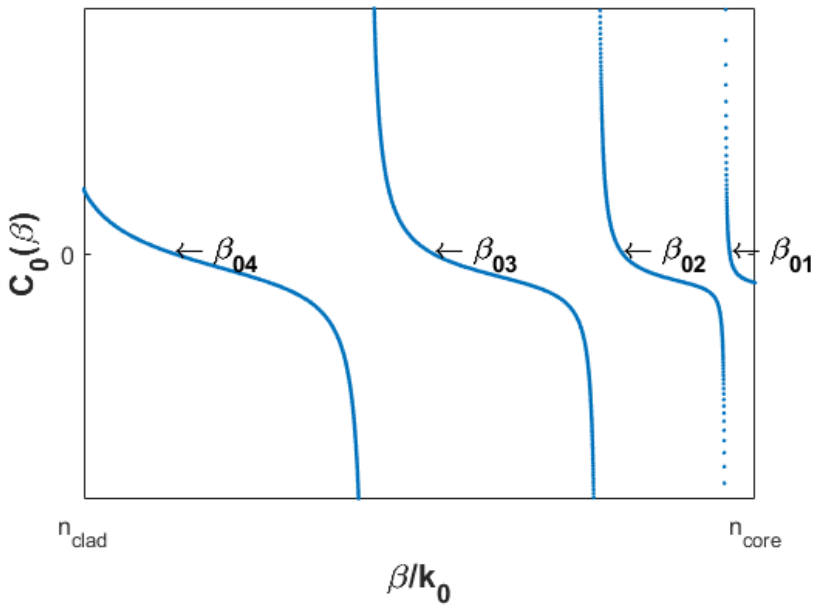

Figure 2.1: Numerical calculation of the characteristic equation.

If the step size of the discrete β values is chosen too large, there can be two solutions within two consecutive points. In such intervals, the algorithm will under-count the number of LP modes. It is possible to test the accuracy of the results by trying smaller step sizes and observing when the found number of modes starts to converge. Another test is to compare the number of modes found by the simulation to the number of modes estimated by the "V number" of the fiber, $N_{\text{modes}} \approx V^2/2$ where $V = 2\pi a \text{NA}/\lambda$. In this study, the step size is justified using these two methods.

The actual field distributions can be calculated from the β_{mp} solution values using Eq. 2.16 and 2.17. Fig. 2.2 visualizes two LP modes for $z = 0$ and $t = 0$.

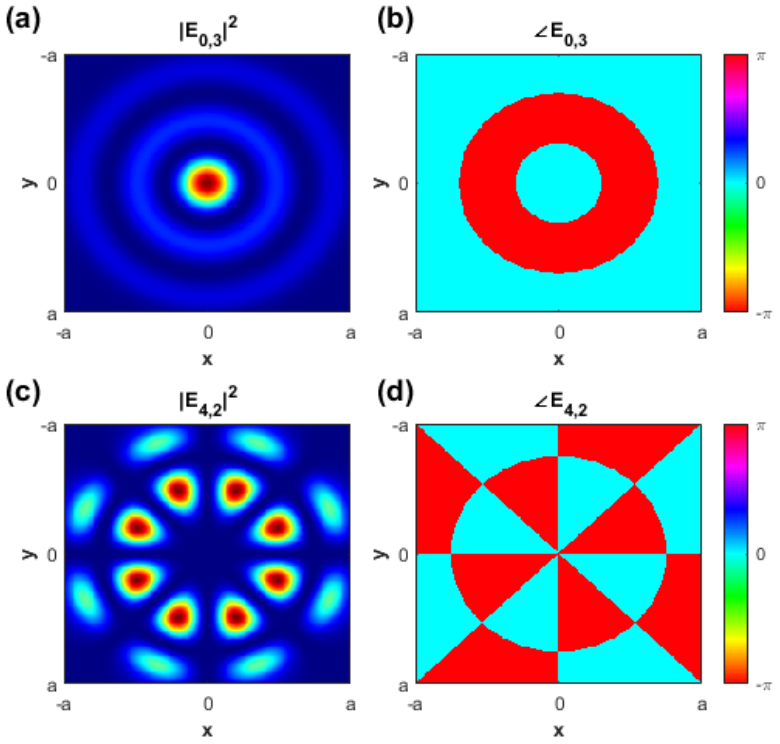

Figure 2.2: Intensity and phase distribution for two example LP modes. The upper one is for even $m = 0$, $p = 3$. The lower one is for odd $m = 4$, $p = 2$. **(a)** Intensity of the even mode of $m = 0$, $p = 3$. **(b)** Phase of the even mode of $m = 0$, $p = 3$. **(c)** Intensity of the odd mode of $m = 4$, $p = 2$. **(d)** Phase of the odd mode of $m = 4$, $p = 2$.

At the output of the fiber, the LP modes will obtain a phase shift due to the propagation. At an arbitrary coordinate z, the LP mode will still have the same intensity as

long as it is the only mode excited. Fig. 2.3 illustrates the intensity distribution of a single LP mode along the $z = 0$, $z = 3\mu$m and $x = 0$ planes. Since the LP mode obtains a phase shift as it propagates, the real part of the complex field will alternate as shown in Fig. 2.4 for the same planes.

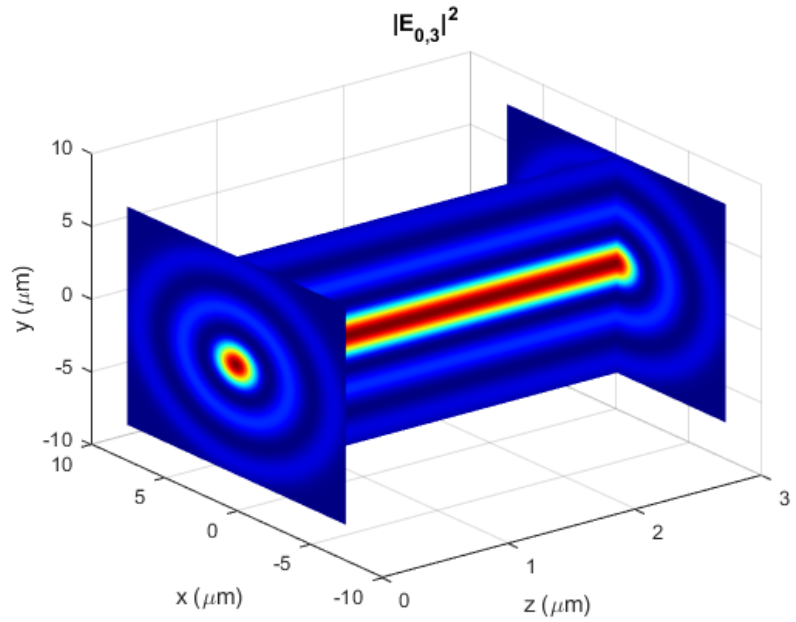

Figure 2.3: Intensity of the LP mode of $m = 0$ and $p = 3$ along the $z = 0$, $z = 3\mu$m and $x = 0$ planes.

A random speckle pattern can be generated using random excitation levels for each LP mode. This is programmed by generating randomly each c_{mp} as a complex normal random variable. Fig. 2.5 illustrates the intensity distribution of a random speckle pattern along the $z = 0$, $z = 1$mm and $x = 0$ planes. If a camera is placed at the end of a 1mm MMF, the image should be similar to the distribution in the $z = 1$mm plane. Similarly, Fig. 2.6 shows the phase of the speckle pattern in the same planes.

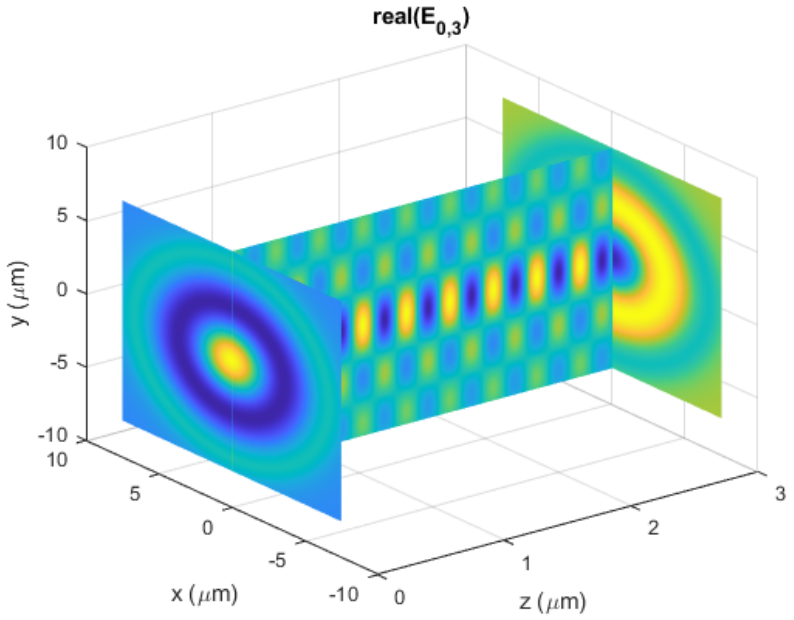

Figure 2.4: Real part of the LP mode field of $m = 0$ and $p = 3$ along the $z = 0$, $z = 3\mu$m and $x = 0$ planes.

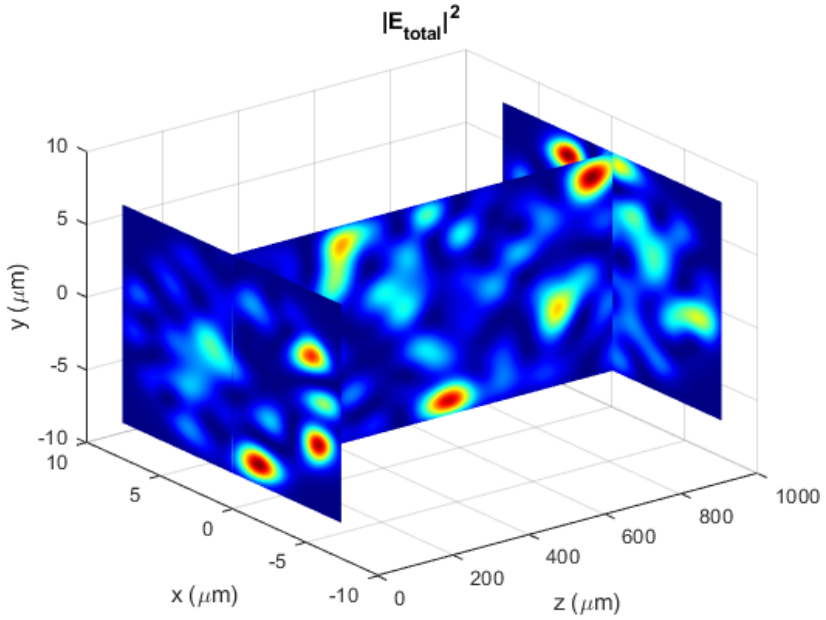

Figure 2.5: Intensity of a random speckle pattern along the $z = 0$, $z = 1$mm and $x = 0$ planes.

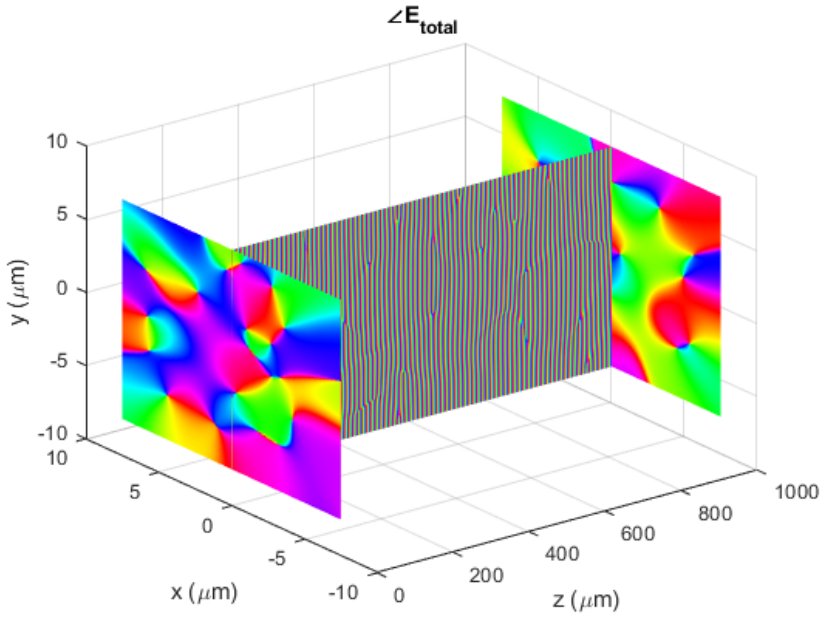

Figure 2.6: Phase of a random speckle pattern along the $z = 0$, $z = 1$mm and $x = 0$ planes.

In the real experiments, the coefficients c_{mp} are not random numbers. The values are determined by the coupling at the input of the fiber which is why the spatial distribution of the field at the fiber input is critical. If a beam is focused in a circular region within the fiber, the coupled field will be an approximation to that field as a summation of the LP modes. Fig. 2.7 shows an example of a field coupling into the fiber. Fig. 2.7(a) shows the field distribution arranged right before the fiber input. Fig. 2.7(b) shows the coupled field inside the fiber which should propagate without energy loss. Fig. 2.7(c,d) show the field intensities after propagating 1mm and 1m in the fiber, where the energy starts to spread around within the core.

If a different MMF with more number of modes was used instead of the MMF used in Fig. 2.7 which has 34 modes, the field which couples into the MMF would be much similar to the field provided just before the fiber entrance. Fig. 2.8 shows the same field coupling and propagation for a fiber with 557 modes. Even though the propagation distances are similar in Fig. 2.7 and Fig. 2.8, the intensity distributions are much different due to the difference in the fiber parameters which are given in the captions.

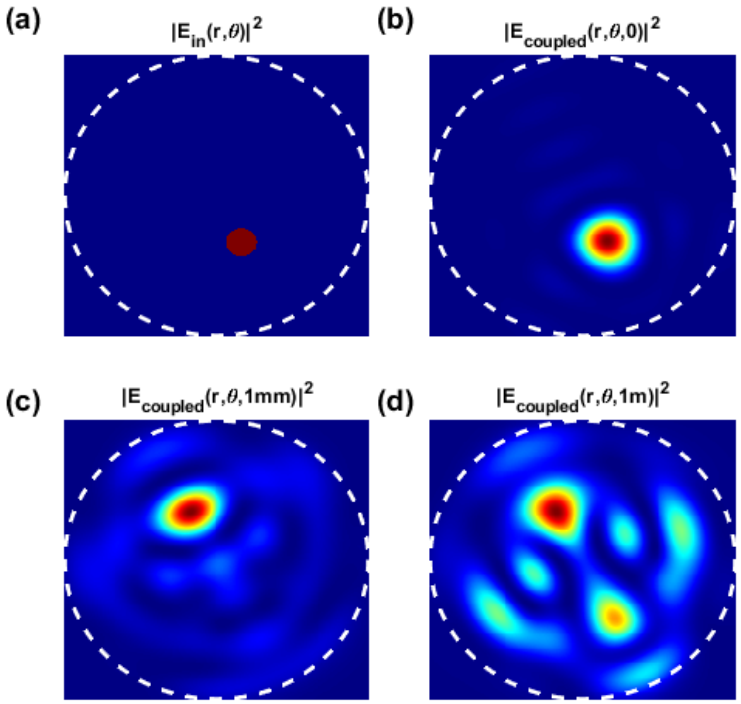

Figure 2.7: Coupling of a field into and propagating within the MMF described earlier which supports 34 modes with the parameters of $a = 7.5\mu$m, $\lambda = 500$nm, NA $= 0.12$. **(a)** The incoming field intensity distribution. The field intensity distribution within the fiber at **(b)** $z = 0$, **(c)** $z = 1$mm, and **(d)** $z = 1$m.

Up to here, all MMF outputs assumed that the LP modes do not transfer energy amongst themselves along the way. This would be true in an idealistic scenario where the materials are perfect and the fiber geometry is completely straight just like the cylindrical geometry used in the theory. To simulate more realistic situations, the mode-to-mode TM, **T**, described in Eq. 2.18 can be altered to a non-identity matrix. All calculations up to here assumed an identity TM. Fig. 2.9 illustrates the difference at the output if a completely random TM was used instead of an identity TM. The speckle patterns for the identity TM and a random TM are clearly different as it can be seen in the figure.

All the calculations until here can be used in most studies involving MMF's and CW lasers. However, in order to study fiber spectrometers, we are interested in the spectral dynamics of a MMF. In order to calculate the output at a slightly different wavelength,

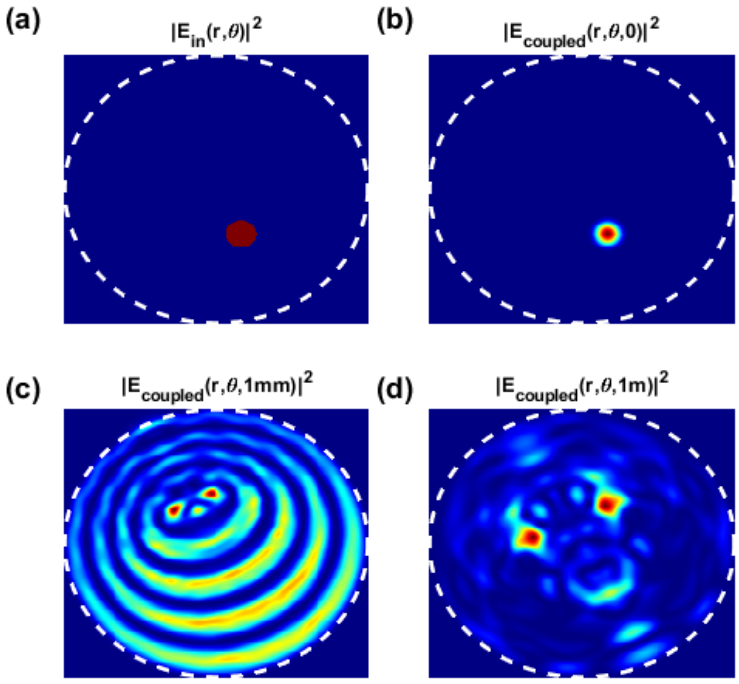

Figure 2.8: Coupling of a field into and propagating within a MMF which supports 557 modes with the parameters of $a = 52.5\mu$m, $\lambda = 1550$nm, NA $= 0.22$. **(a)** The incoming field intensity distribution. The field intensity distribution within the fiber at **(b)** $z = 0$, **(c)** $z = 1$mm, and **(d)** $z = 1$m.

all the calculations starting from the characteristic equation should be done again. Just to plot a graph with wavelength as the independent variable, too many calculations are required which becomes computationally too expensive. This issue can be pushed aside under the assumption that the wavelength range is very small, $\Delta\lambda \ll \lambda_0$ where λ_0 is the central wavelength and $\Delta\lambda$ is the bandwidth of interest. Let λ be an arbitrary wavelength within the range $\lambda_0 - \Delta\lambda/2 < \lambda < \lambda_0 + \Delta\lambda/2$. The bandwidth can be sufficiently small if the following are true:

- Number of LP modes is constant within the range, $N(\lambda) = N(\lambda_0)$
- Spatial profiles of the LP modes are constant, $E_{mp}(r, \theta; \lambda) = E_{mp}(r, \theta; \lambda_0)$
- Mode-to-mode TM is constant, $T(\lambda) = T(\lambda_0)$

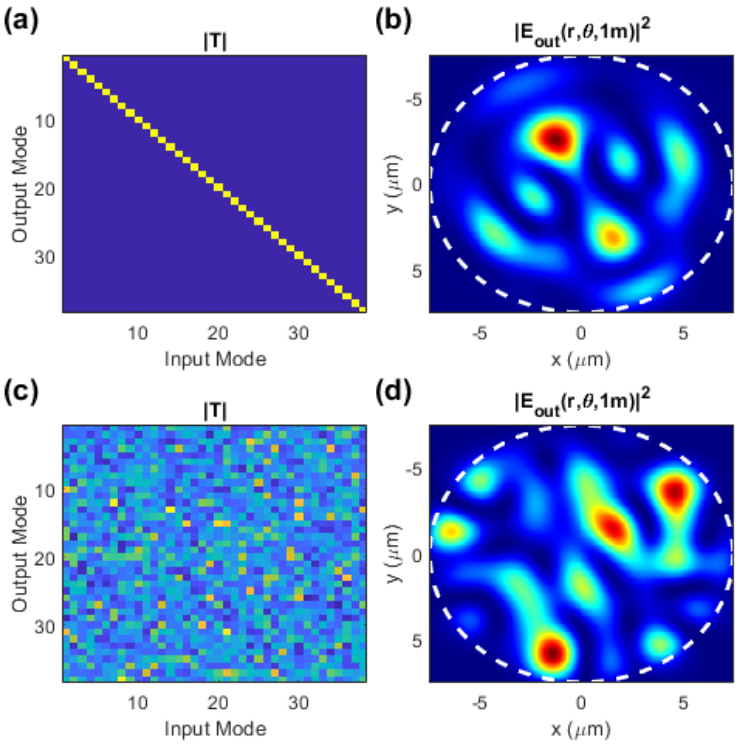

Figure 2.9: The speckle patterns at the output under different TM's for the MMF supporting 34 modes. **(a)** Identity mode-to-mode TM. **(b)** The field intensity distribution at $z = 1$m corresponding to the TM given in (a). **(c)** Random mode-to-mode TM where each element is a complex normal random variable. **(d)** The field intensity distribution at $z = 1$m corresponding to the TM given in (c).

Under these circumstances, the only difference while calculating the whole field in the MMF, comes from the phase term in $\mathbf{E}_{mp}$. At $t = 0$, the difference can be written as

$$\mathbf{E}_{mp}(\lambda) = |\mathbf{E}_{mp}(\lambda_0)| e^{i \arg(\mathbf{E}_{mp}(\lambda_0)) \frac{\lambda_0}{\lambda}}. \tag{2.19}$$

Using this new technique is very convenient for computational resources. Fig. 2.10 shows the spectral dependence of the speckle patterns using a random TM for a 34-mode MMF. Fig. 2.11 shows the same figure for a 557-mode MMF which is closer to the MMF used in our experiments: $a = 52.5\mu$m, $NA = 0.22$, $L = 20$m.

The idea of MMF based spectrometer comes here. Since the speckle patterns change

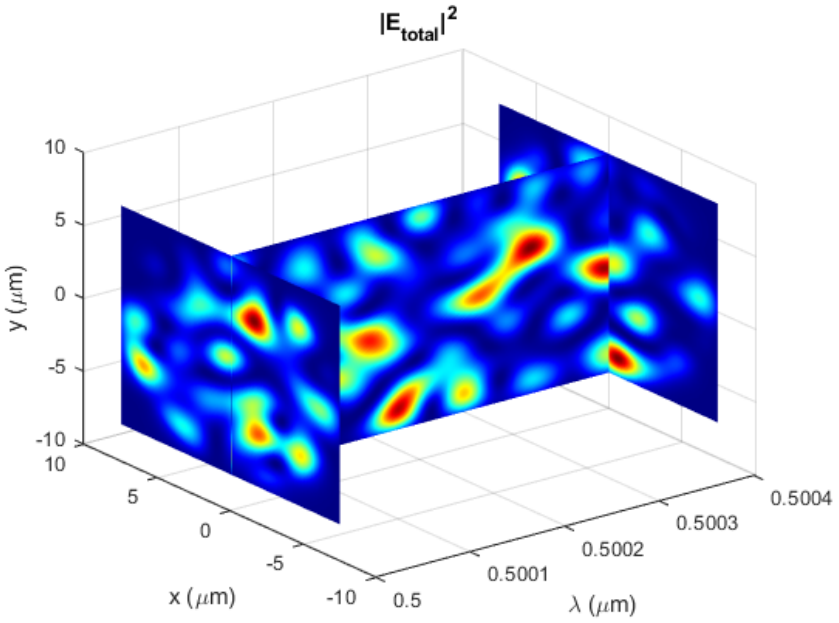

Figure 2.10: Spectral dependence of the speckle intensity patterns for the MMF with 34 modes.

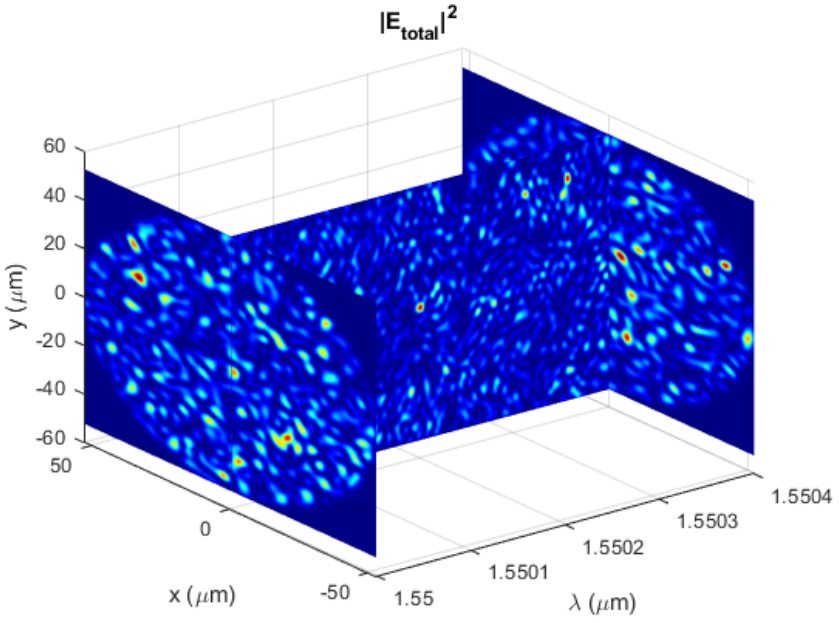

Figure 2.11: Spectral dependence of the speckle intensity patterns for the MMF with 557 modes.

as the wavelength changes, as it can be seen in Fig. 2.11, it is possible to construct a spectrometer. The similarity between two speckle patterns can be calculated using the Pearson correlation. Fig. 2.12 shows three different speckle patterns at different wavelengths. The Pearson correlation between (a) and (b) is around 0.95 while the correlation between (a) and (c) is around 0.22. Clearly, as the wavelength changes, the correlation drops.

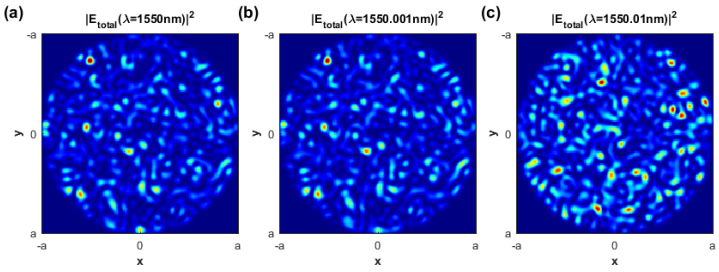

Figure 2.12: Speckle field intensities at the output of 20m long 557 mode MMF with a random TM at different wavelengths of **(a)** $\lambda = 1550.00$nm, **(b)** $\lambda = 1550.001$nm and **(c)** $\lambda = 1550.010$nm.

The correlation drop as the wavelength is changed can be visualized better with a correlation versus wavelength variation graph. The speckle patterns at different wavelengths are used to calculate the curves in Fig. 2.13. If a spectrometer was constructed using this MMF, the spectral resolution of that spectrometer would be close to the full width at half prominence (FWHP) value of this curve. The FWHP is similar to full width at half maximum (FWHM) but the prominence accounts for the situation that the curve never reaches zero. FWHP uses the peak value and the zero-slope value where the peak ends to calculate the full width of the peak. If FWHM was calculated from the curves in the graph, the width would be larger than expected because the curves never decrease down to zero. Fig. 2.13 illustrates the speckle correlation curves for the identity TM case and random mode-to-mode TM case. The FWHP for the random TM is smaller which is an indication of the dependence of the resolution on the TM.

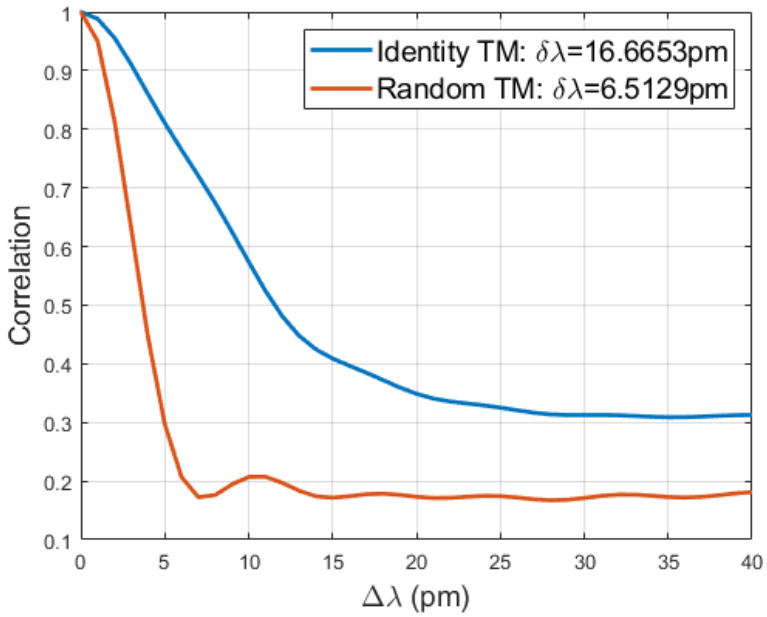

Figure 2.13: Speckle correlation values averaged over lambda for identity and random TM cases. The FWHP of the curves are given in the legend.

CHAPTER 3

EXPERIMENTAL SETUPS

3.1 Phase-only Modulation Setup

The experimental setup for phase-only modulation can be seen in Fig. 3.1. A step-index MMF with a 105 μm core diameter, and NA=0.22 is used. Two different lenghts of MMF's are used at different stages, a 2m fiber and a 20m fiber. The 20m MMF provides a direct comparison with the pioneering study in [9]. The MMF was laid on the optical table and kept as stable as possible without the use of any additional stabilization mechanisms. A wavelength selectable laser (SANTEC WSL-100) that operates at the telecom range, 1550 nm, was used throughout the experiments. The laser output is coupled into a polarization maintaining fiber which ensures that the incoming spatial beam profile is fixed. Then, the beam is coupled to free space and expanded for phase modulation using a phase only SLM which functions properly with linear polarization (Holoeye Pluto-Telco). A blazed grating is always added to the intended phase pattern to eliminate 0^{th} diffraction order. After the SLM, the beam is focused by a lens (L1 in the schematic) and the 0^{th} order is filtered by an aperture. Only the 1^{st} order couples into the MMF after a second lens (L2) and a fiber port collimator that contains a third lens (Input Coupler) with a small focal length of 8.12mm. The output of the MMF is recorded using a InGaAs monochrome camera (Allied Vision Goldeye SWIR-TEC). A typical speckle pattern can be seen in the top right corner of Fig. 3.1.

This setup is verified to function properly by obtaining a focal point within the speckle pattern using a feedback based iterative algorithm. The results show that a focal point at the end of the fiber can be obtained through such algorithms which validates that

the phase modulation is able to shape the wavefront of the beam and the impact on the speckle pattern can be observed.

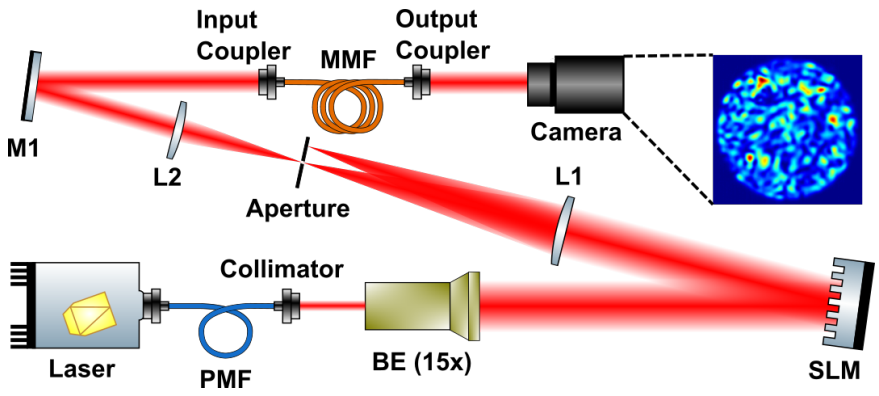

Figure 3.1: Phase-only modulation setup. A typical speckle pattern obtained from the setup is also shown.

3.1.1 Wavefront Shaping Through a Multimode Fiber

In order to focus the light at a specific point within the speckle pattern, the algorithm developed in [26] is adapted. The algorithm is a feedback based iterative optimization of the target region intensity. This algorithm changes the value of all pixels on the SLM in each iteration and therefore the effect of the new modification is much more apparent compared to pixel based algorithms. Also, as reported in [26], the optimization is faster compared to exhaustive-type algorithms. For the setup constructed here, a visible focal point can be obtained with around 1000 trials. The corresponding time required is dependent on the SLM speed.

The flow of the algorithm is shown in Fig. 3.2. Let the phase displayed on the SLM in the n^{th} iteration be Φ_{n}. In order to find the phase for the next iteration, a temporary phase, Φ_{temp}, is calculated as

$$\Phi_{\text{temp}}(x,y) = \arg\left[(1-\xi)e^{i\Phi_{\text{n}}(x,y)} + \xi e^{i(kx\cos\alpha + ky\sin\alpha + \theta)}\right] \tag{3.1}$$

where x and y are the coordinates of the SLM pixels, and all other variables are uniform random variables generated again at each trial. ξ is generated from the range

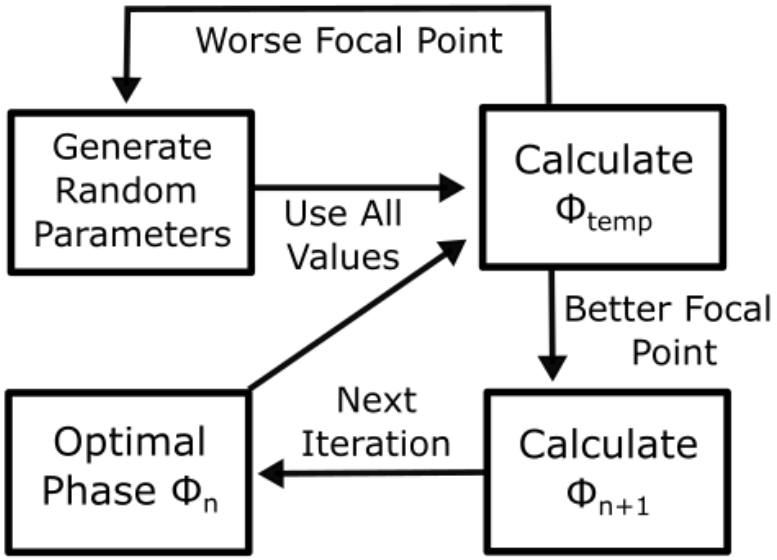

Figure 3.2: Algorithm flow of the focal point optimization.

$[0, 1/2]$. α and θ are random phases in the range $[0, 2\pi)$. k is generated from the interval $[0, k_{\text{max}}]$ where k_{max} depends on the setup parameters as explained in [26]. The temporary phase is assigned to the next iteration phase, $\Phi_{\text{n+1}}(x, y) = \Phi_{\text{temp}}$, if the target intensity is higher, $I_{\text{temp}}^{\text{target}} > I_{\text{n}}^{\text{target}}$ than the previous intensity. Otherwise, no assignment is made and the Φ_{temp} is generated again with new random values. Fig. 3.3 illustrates the optimization process with the SLM phase patterns and the corresponding speckle patterns at different iterations.

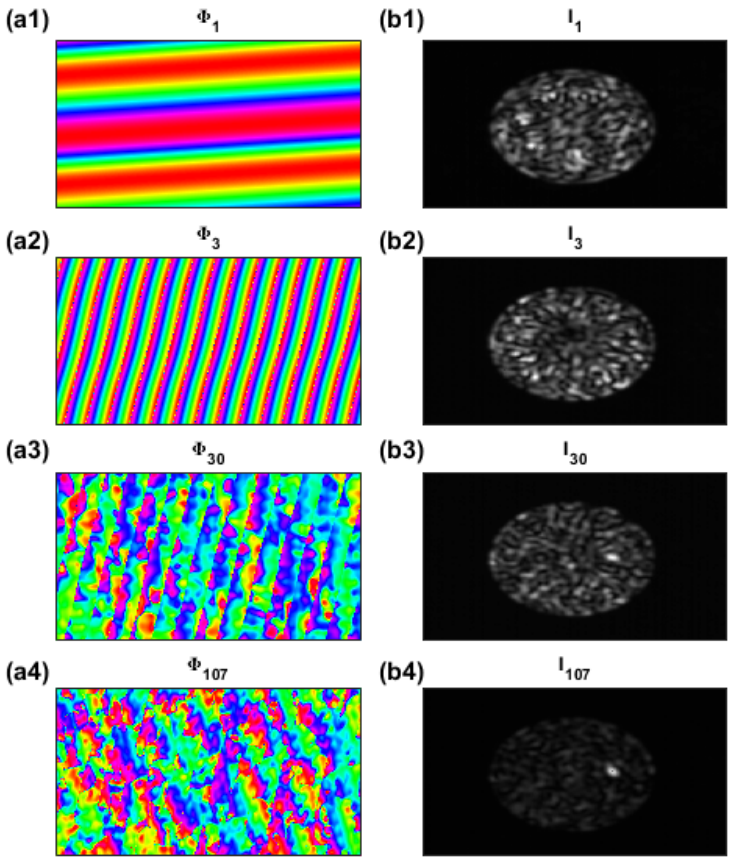

Figure 3.3: Optimization of the target intensity. **(a1-4)** The phase distributions on the SLM at various iterations. **(b1-4)** The corresponding speckle patterns which are progressively more focused in the targets spot.

3.2 Amplitude and Phase Modulation Setup

Since the SLM works as a phase-only modulator, modulating the amplitude and phase independently requires a special technique [51]. In order to modulate the complete complex field, certain modifications in the setup are required as in Fig. 3.4. The same MMF, SLM, laser, and camera are used while the 4-f system after the SLM filters out the high spatial frequencies and assures amplitude and phase modulation. The amplitude modulation of this setup is verified using a temporary setup shown in Fig. 3.5. An extra lens (16mm) is used in this setup to ensure that the field modulated by the SLM itself and not its Fourier (focused version) enters the fiber.

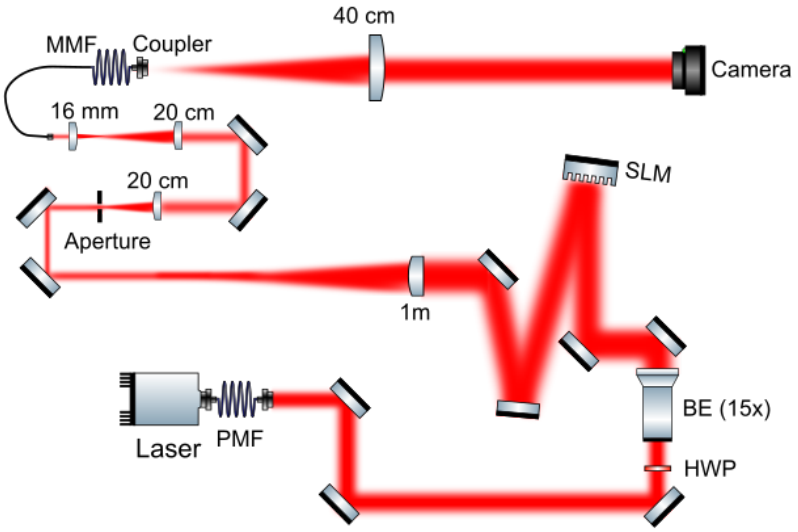

Figure 3.4: Amplitude and phase modulation setup.

3.2.1 Super-pixel Technique

The SLM used here is phase-only which means that the field amplitude is not altered whatever the SLM pixel value is chosen. In order to independently control both the amplitude and phase distribution, a super-pixel technique is used [51]. There are several techniques used in different situations in the literature [51–55]. The most appropriate technique [51], and used for MMF studies in [56] is adapted here. This section is written to develop an intuitive understanding of the technique.

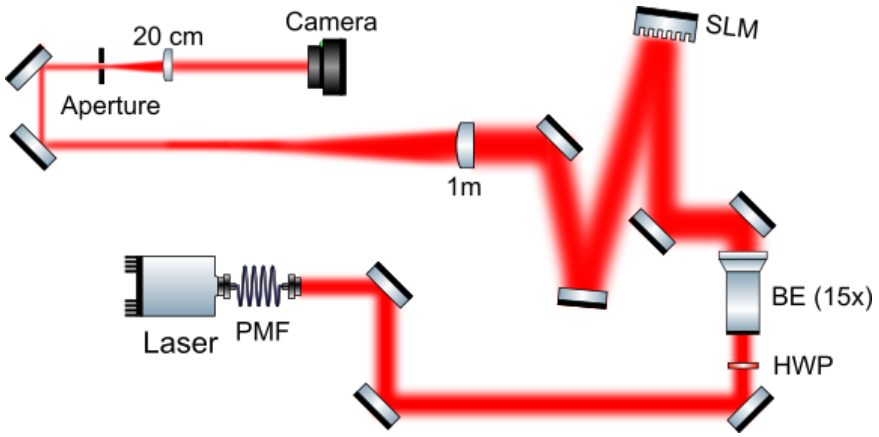

Figure 3.5: Amplitude and phase modulation verification setup.

Imagine there is a complex electric field distribution $E_{\text{Intended}}(x, y) = A(x, y)e^{i\psi(x,y)}$ intended to be displayed at the fiber input face where $A(x, y)$ is the field amplitude and $\psi(x, y)$ is the field phase. For now, assume the intended amplitude has the shape of the capital character "A" as shown in Fig. 3.6(a) and the phase has the shape of the capital character "B" as shown in Fig. 3.6(b).

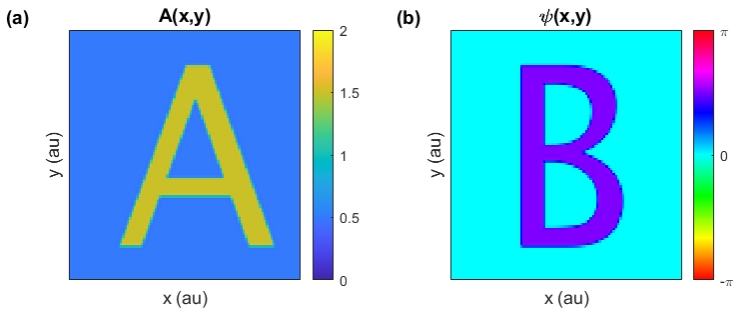

Figure 3.6: **(a)** Amplitude and **(b)** phase of the intended field.

The important step of this technique is to create a super-pixel consisting of 2x2 pixels for each pixel in the complex field as drawn in Fig. 3.7. This doubles the required number of pixels for the same resolution but it allows for complete control over the amplitude and phase independently. The phase values $\phi_1(x, y)$ and $\phi_2(x, y)$ to be written on a single super-pixel are determined from the intended amplitude $A(x, y)$

and phase $\psi(x, y)$ as

$$\varphi_1(x, y) = \psi(x, y) - \arccos(A(x, y)/2), \tag{3.2}$$

$$\varphi_2(x, y) = \psi(x, y) + \arccos(A(x, y)/2). \tag{3.3}$$

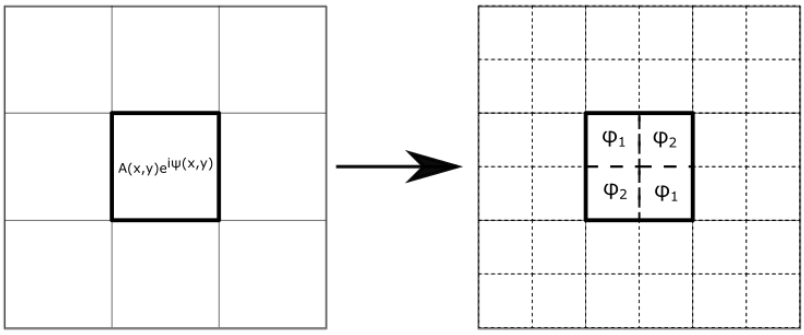

Figure 3.7: A sketch representing the formation of a super-pixel. A single pixel in the complex field distribution corresponds to a region of 2x2 region after the formation.

Since a low pass filter will basically sum these fields within the super-pixel the final field will be $E(x, y) = e^{i\varphi_1} + e^{i\varphi_2}$ which can be simplified to $E(x, y) = Ae^{i\psi}$. Therefore, low pass filtering the field is essential in obtaining the desired amplitude and phase modulation. When the super-pixels are created for the intended complex field in Fig. 3.6, the phase array to be displayed on the SLM is calculated as shown in Fig. 3.8(b). The amplitude distribution after the phase-only SLM is as uniform as the beam, shown in Fig. 3.8(a).

In fact, the traces of the "A" and "B" patterns can probably be seen on the phase distribution depending on paper print quality of this thesis or the monitor resolution displaying the digital version of this thesis. Under the right scale, my monitor averages out neighbouring pixels resulting in a natural filter before the reader's eyes. In the lab, to low-pass filter the field, a Fourier transformation is necessary. The Fourier of an optical field can be taken using a single lens [57]. The electric field at the post focal plane is the Fourier of the electric field at the prior focal plane. Using this prop-

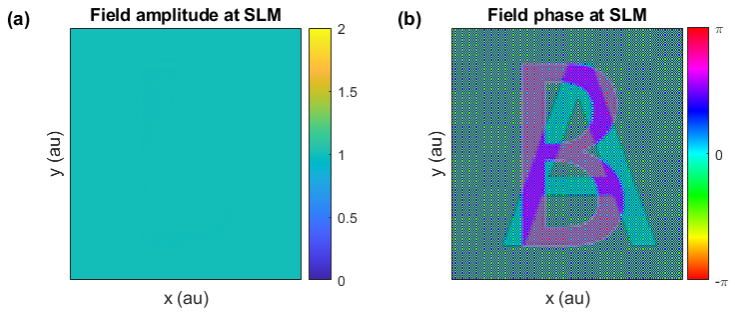

Figure 3.8: **(a)** Amplitude and **(b)** phase of the field right after the SLM.

erty, the $f = 1$ m lens in Fig. 3.5 takes the Fourier of the phase-only modulated field because the distances between the SLM, lens and iris/aperture are all 1 m. For the sake of this section, the Fourier of the intended field is taken using Fast-Fourier Transform numerically on MATLAB. The results obtained after taking the Fourier transform are depicted in Fig. 3.9: (a) the logarithm of field amplitude at the focal plane, (b) the phase of the same field, (c) the spatial filter that an aperture of that particular size would create, (d) the logarithm of the field amplitude after the filter. The phase of the filtered field is the same as the phase of the field before filtering because the filter is a binary amplitude filter.

The second lens in Fig. 3.5 takes another Fourier transform which can be considered as an inverse Fourier (except for a flip). The field at the post focal plane of the second lens will be the filtered field which is expected to be similar to the intended complex field. Fig. 3.10 shows the amplitude (a) and phase (b) of the obtained field at the post focal plane of the second lens.

The cut-off of the low pass filter, or in the experiments, the aperture size, should be arranged such that there is a clear and sharp intensity distribution. Fig. 3.11 shows the amplitude and phase of the obtained field under various aperture size situations.

The aperture should be small enough to filter out the high frequency corresponding to a period of two pixels which comes from the super-pixel division and large enough to generate a clear and sharp image. Just as important as the aperture size, is the aperture position whose effect is shown in Fig. 3.12. The obtained fields for the slightly displaced aperture positions show the importance of the aperture alignment.

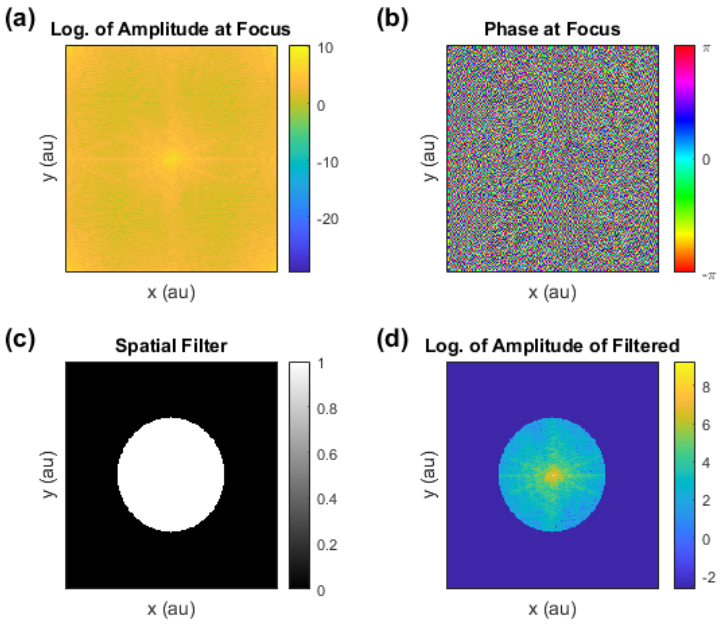

Figure 3.9: **(a)** Amplitude and **(b)** phase of the field at focal plane, **(c)** the low-pass filter shape and **(d)** the filtered amplitude of the field. The phase of the image is unaltered with this binary amplitude filter.

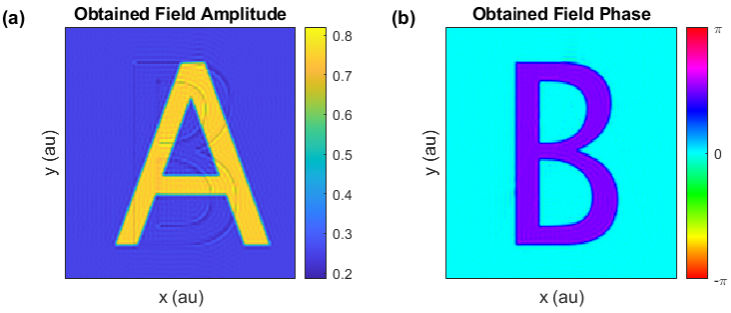

Figure 3.10: **(a)** Amplitude and **(b)** phase of the obtained field.

The super-pixel technique explained in this section allows for independent amplitude and phase modulation using the phase-only SLM. This technique is used in the later sections to generate the field distributions of LP modes of the MMF in use.

The figures in this section are generated numerically on MATLAB but the same procedure is followed experimentally. At all points in this study, the phase array to be displayed on the SLM is added with a blazed grating which just shifts the Fourier image to the 1st order of the grating. Also, in the experiments, instead of using a 2x2

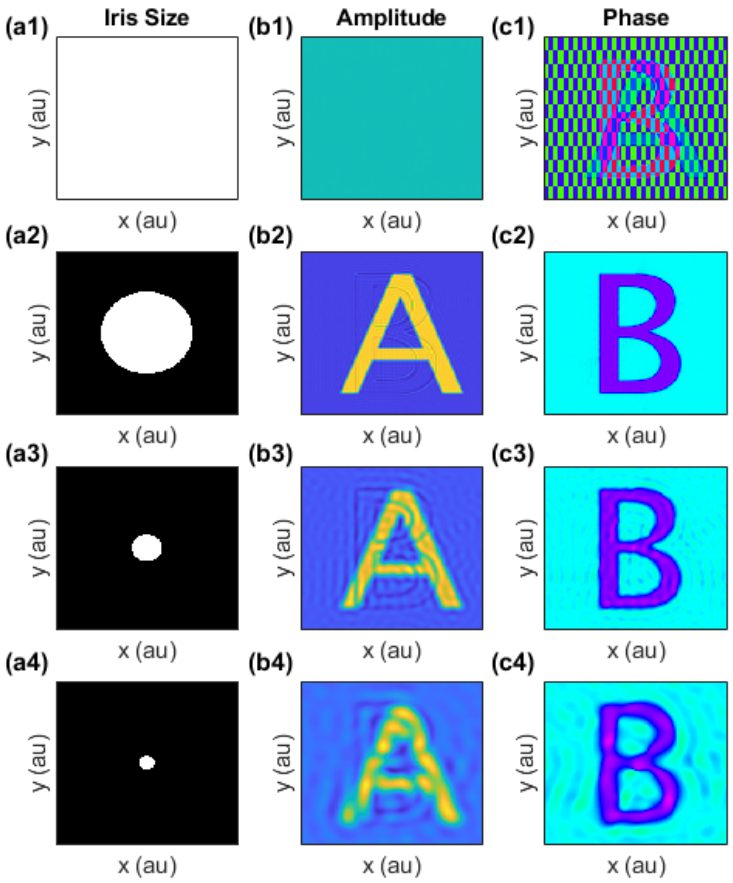

Figure 3.11: Different aperture sizes **(a1-4)** and the amplitude **(b1-4)** and phase **(c1-4)** of the corresponding obtained field.

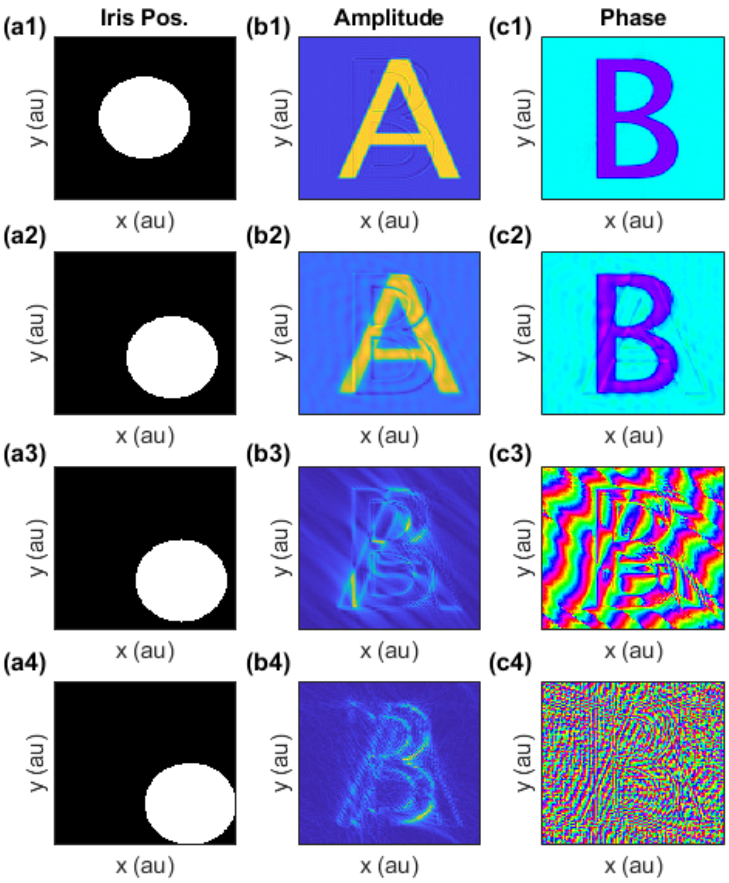

Figure 3.12: Different aperture positions **(a1-4)** and the amplitude **(b1-4)** and phase **(c1-4)** of the corresponding obtained field.

super-pixel, a 6x6 super-pixel is created with 4 regions in a similar manner because it is found to be the optimal case in a previous study [56].

There is another critical point when aligning the experimental setup. It is very important that the fiber input plane is exactly at the post focal plane of the last lens ($f = 16$mm) in Fig. 3.4. Otherwise, an unintended field distribution will enter the fiber. To avoid such an issue, the following alignment procedure is applied. Two amplitude and phase modulated fields are generated as shown in Fig. 3.13. Fig. 3.13(a) is an amplitude distribution where the inner region is illuminated and the outer region is dark. In this case, the majority of the beam should enter the fiber. Fig. 3.13(b) is an amplitude distribution where the outer region is illuminated and the inner region is dark. In this situation almost no beam should enter the fiber. The size of the fiber core in SLM pixel units can be calculated using the magnification of the laser beam after all four lenses in the setup, the fiber core size and the SLM pixel size.

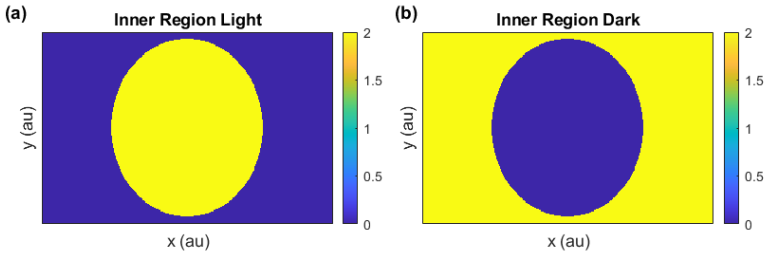

Figure 3.13: Field amplitudes used for fiber alignment. **(a)** Inner region has a non-zero amplitude while the outer region has a zero amplitude. For this input, the coupled power should be maximum. **(b)** Outer region has a non-zero amplitude while the inner region has a zero amplitude. For this input, the coupled power should be minimum.

When aligning the x-y position of the fiber input, it is sufficient to either maximize the first field's coupled power, or minimize the second field's coupled power. However, if the z position of the fiber is not optimal (at exactly the post focal plane of the last lens), it would not be possible to maximize the first and minimize the second simultaneously. So, the z position and the x-y position should be adjusted until both situations are optimized simultaneously, the first field having a high coupled power and the second field having a low coupled power.

If the super-pixel technique was not adopted and amplitude modulation was not pos-

sible, it would be harder to align the fiber in a 4-lens setup. An alignment procedure similar to the one explained should be developed. The pixels in the inner region should affect the speckles while the outer region pixels have no effect. Patterns displayed on the SLM should somehow reflect this effectiveness of the inner and outer regions.

3.3 Phase Conjugation Setup

Phase conjugation is widely used in the MMF studies [31, 35, 36, 56, 58–60] because with the phase information, the input-output correspondence can be estimated with a linear relationship in small fibers. The phase conjugation setup shown in Fig. 3.14 is an interferometric measurement of the speckle patterns. There is an external additional optical path from which unmodified laser beam reaches the camera. This external reference beam interferes with the output of the fiber. The phase delays are given by the SLM on top of the intended complex input field.

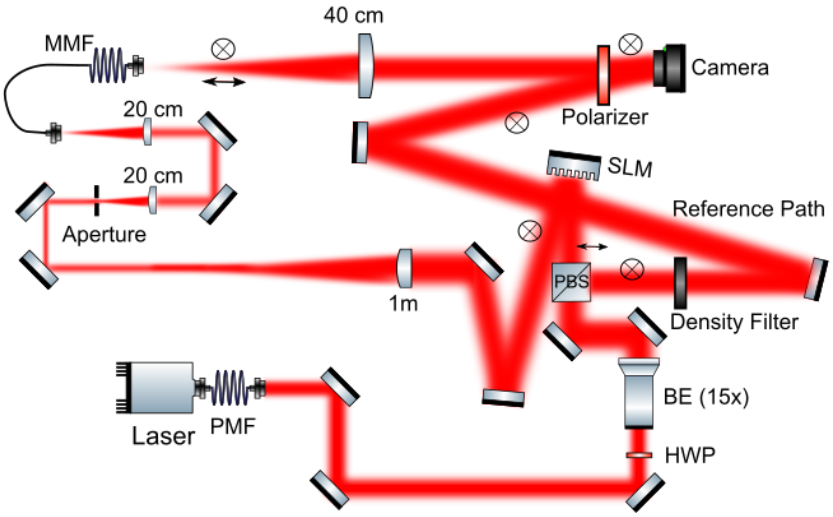

Figure 3.14: Phase-only modulation setup.

A single shot measurement leads to an intensity-only measurement. In order to measure the complex field, an interferometric measurement is required. For the interferometric measurement, phase delays of $\alpha \in \{0, \pi/2, \pi, 3\pi/2\}$ are given and the output

intensity patterns are measured. The intensity at the camera can be calculated as

$$I_\alpha = |E_{\text{ref}} + E_{\text{fiber}} e^{i\alpha}|^2 \tag{3.4}$$

where $E_{\text{fiber}} = Ae^{i\theta}$ is the field coming from the fiber output and $E_{\text{ref}} = A_0$ is the field coming from the reference path. The reference field also defines the reference phase which is why the beam should be as clean and uniform as possible. α is the additional phase given by the SLM intentionally. After recording the intensity under different phase delays, the complex field can be calculated by

$$E_{\text{complex}} = \sum_\alpha I_\alpha e^{-i\alpha} = 8A_0 A e^{i\theta} = 8E_{\text{ref}} E_{\text{fiber}}. \tag{3.5}$$

It can be seen that the final calculation is only proportional to the desired field if the reference field is uniform. Fig. 3.15 shows the intensities at four different delays and the calculated summation which should be proportional to the desired complex field. The final field qualitatively looks like any other speckle pattern which is an indication of the phase measurement accuracy.

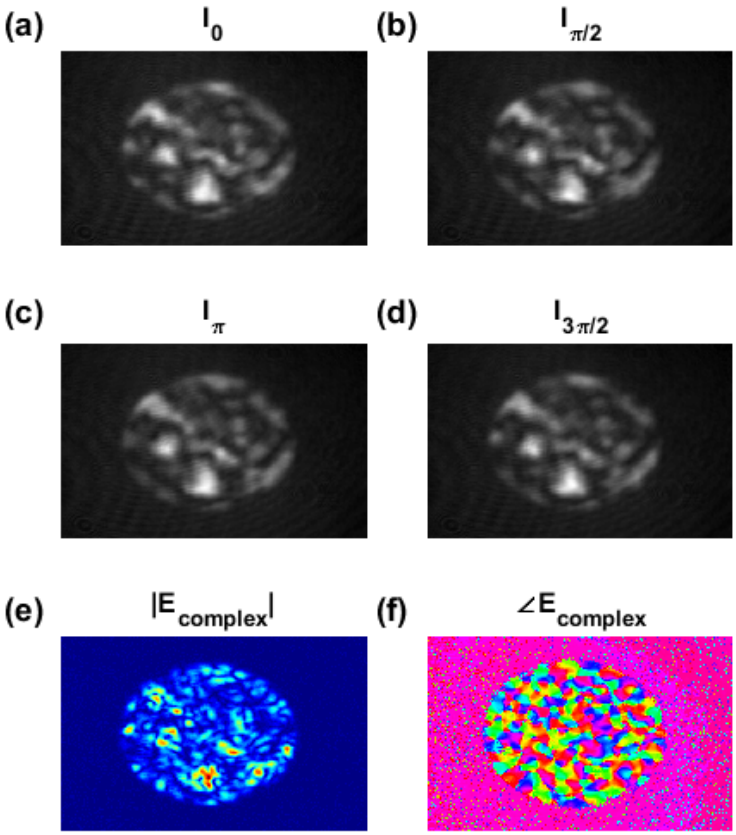

Figure 3.15: The camera images recorded with different phase delays of **(a)** 0, **(b)** $\pi/2$, **(c)** π, and **(d)** $3\pi/2$. The **(e)** amplitude and **(f)** phase of the calculated fiber output.

CHAPTER 4

METHODS AND RESULTS

Before this study was conducted, MMF based spectrometers were already known in the literature [7–16]. The first findings of this study verify the results in the literature. The authors of [9] use fibers with core diameter 105μm, or $a = 52.5\mu$m, NA $= 0.22$ and $L = 20$m in the telecom range. Here, the same MMF have been used. Also, it is shown that the spectral resolution scales linearly with the fiber length [9]. Thus, a MMF with the same parameters but $L = 2$m is also used. In order to calculate the spectral resolution, Pearson correlation is used in this study and Pearson correlation is very similar to a custom definition used by Redding et. al. in [9]. Both correlation definitions can be seen to give similar results in Fig. 4.1, where the correlation curves for 2m and 20m fibers can be seen.

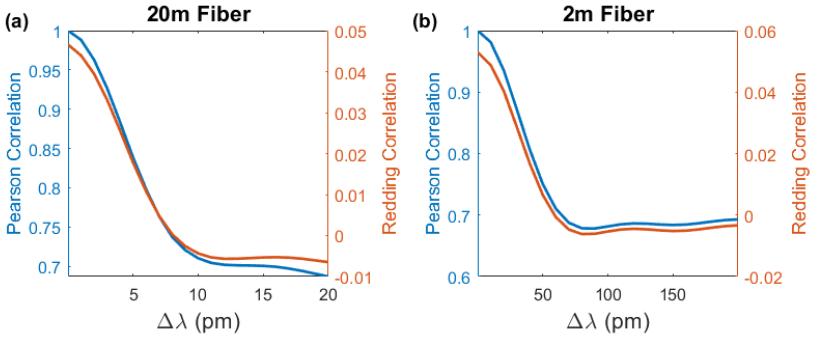

Figure 4.1: Correlation curves for the original spectrometers. **(a)** For the 20 m long fiber, the Pearson correlation curve, in blue, and the Redding correlation curve, in red. The FWHM of Redding is 8.63 pm and the FWHP of Pearson is 9.73 pm. **(b)** For the 2 m long fiber, the Pearson correlation curve, in blue, and the Redding correlation curve, in red. The FWHM of Redding is 70 pm and the FWHP of Pearson is 63.9 pm.

In this study, the Redding correlation becomes incalculable after certain procedures. But Pearson correlation is still useful in those cases. As a result, the Pearson correlation will be used in the upcoming analyses. Also, to calculate the resolution from the Redding correlation curve, normally, the zero-crossing point and/or FWHM is used [9]. However, to calculate the width of the Pearson correlation curve, FWHM is not appropriate because it never reaches zero. An alternative definition is the full width at half prominence (FWHP) which can be calculated using the built-in function `findpeaks` on MATLAB. FWHP calculation uses the zero-slope points instead of zero-crossing points. It can be seen from Fig. 4.1 that both definitions are very similar. The resolutions are summarized in Table 4.1.

Table 4.1: Spectral resolution values of the original spectrometers.

	FWHM of Redding Corr.	FWHP of Pearson Corr.	Literature
2 m	63.9 pm	70 pm	-
20 m	8.63 pm	9.73 pm	10 pm [9]
100 m	-	-	1.5 pm [10]

4.1 Fiber Spectroscopy Using Orthogonal Input Wavefronts

Unlike conventional MMF-based spectrometers where the wavefront of the incoming beam is kept fixed [9, 10, 13–15], in the following methods, it is phase-modulated before entering the MMF using the setup given in Fig. 3.1 with the objective of enhancing the resolution. For each incoming spectrum to be analyzed by the spectrometer, multiple snapshots of the output speckle pattern are recorded under various phase modulations via the SLM, each taking milliseconds depending on the speed of the SLM and camera. As a result, we obtain additional frequency dependent degree of control that leads to increased resolution. Although this gives a wider range of information, it does not directly enhance the resolution of the spectrometer. The new information is used in two different, simple yet fast, processing steps to create images that are more sensitive to changes in the spectrum, explained in the following subsections. The SLM patterns are selected from an orthogonal basis, for which, vectors are

drawn from a Hadamard basis [27, 29]. In fact, the speckle patterns at the output of a MMF are shown to be sparse even if the input images are not selected from a random basis [61]. As long as the inputs result in sufficiently different speckle patterns as if they could have been the outputs of different fibers, they can be used. For this reason, any choice of SLM patterns (other than Hadamard based patterns) might be appropriate if the speckle patterns are not similar.

A one-dimensional vector drawn from a Hadamard matrix is reshaped as a square. Then, this square matrix is resized to have the same size as the SLM screen. Four of these patterns obtained from four different Hadamard vectors are displayed on the SLM and the corresponding output speckle patterns are recorded for a range of wavelengths. An example set of Hadamard-based SLM patterns and corresponding speckle patterns obtained for a single wavelength are shown in Fig. 4.2(a) and Fig. 4.2(b), respectively. In our measurements, we observe that four structured SLM patterns are sufficient to nearly double the resolution that only takes 16.6x4=66.4 ms with our equipment, which is much faster than a scanning grating that is employed in a conventional spectrometer.

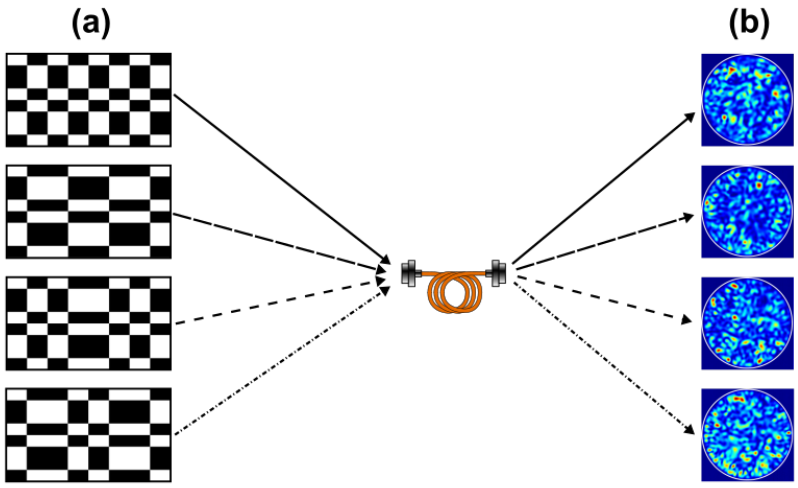

Figure 4.2: An illustration of the spatial filtering method. **(a)** The patterns displayed on the SLM for phase modulation. Each pattern is created using a vector drawn from the Hadamard matrix. The black regions represent 0 phase modulation while white regions represent π modulation. **(b)** The speckle patterns obtained at a single wavelength for the corresponding SLM patterns.

4.1.1 Spatial Filtering

The first method for post-processing, spatial filtering for this section, is implemented after recording the speckle patterns for a number of different SLM patterns at all wavelengths of interest. This filtering method is visualized in Fig. 4.3(c-d). After adding all the speckle patterns obtained for different vectors, the image is filtered using a band-pass filter. The cut-off frequencies of the filter are varied and the best set of parameters are chosen in the end. An example image for a single wavelength after such a procedure is shown in Fig. 4.3(d). After the filter, the image includes speckle grains within a certain range of size (determined by the cut-offs). Intuitively, the filtering affects the decorrelation length because of the underlying LP mode structures. LP modes with naturally smaller individual speckles are left in the image. The wavevector, β, values of these LP modes will be more dominant after the filtering. In fact, there are more lobes/structures in the LP modes with high (m, p) values. These LP modes usually have smaller β_{mp} values. So, spatial filtering, indirectly, modifies the effective β_{mp} values within the speckle pattern.

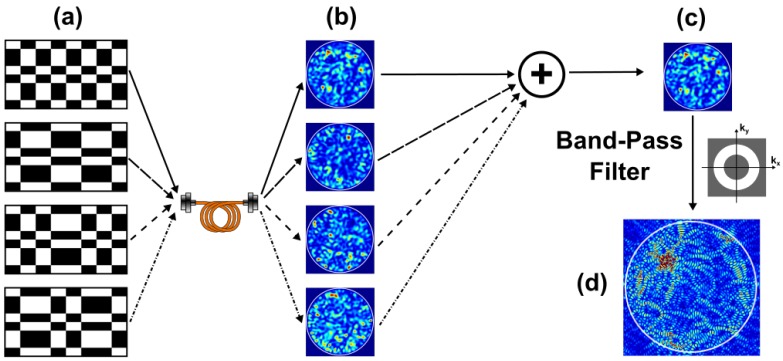

Figure 4.3: An illustration of the spatial filtering method. **(a)** The patterns displayed on the SLM for phase modulation. Each pattern is created using a vector drawn from the Hadamard matrix. The black regions represent 0 phase modulation while white regions represent π modulation. **(b)** The speckle patterns obtained at a single wavelength for the corresponding SLM patterns. **(c)** The obtained images are summed. Afterwards, this summed image is filtered using a band-pass filter. **(d)** The filtered output speckle image at a single wavelength.

To express the technique analytically, let $I_n^{\text{raw}}(\lambda; x, y)$ be the raw output speckle pat-

tern without any filtering obtained for the n^{th} Hadamard vector at λ. The summed image can be expressed as

$$I_m^{\text{sum}}(\lambda; x, y) = \sum_{n=1}^{m} I_n^{\text{raw}}(\lambda; x, y) \tag{4.1}$$

where, m is a positive integer. Next, the summed image is filtered through a band-pass filter which can be expressed as

$$I_m^{\text{filtered}}(\lambda; x, y) = \mathcal{F}^{-1}\{\mathcal{F}\{I_m^{\text{sum}}(\lambda; x, y)\}H(k_x, k_y)\} \tag{4.2}$$

where $\mathcal{F}$ is 2D Fourier Transform and $\mathcal{F}^{-1}$ is its inverse. $H(k_x, k_y)$ is the frequency response of the band-pass filter which can be defined as

$$H(k_x, k_y) = \begin{cases} 0, & \text{if } \sqrt{k_x^2 + k_y^2} < k_{\text{low}} \\ 1, & \text{if } k_{\text{low}} \leq \sqrt{k_x^2 + k_y^2} < k_{\text{high}} \\ 0, & \text{if } k_{\text{high}} \leq \sqrt{k_x^2 + k_y^2} \end{cases} \tag{4.3}$$

This filtering is performed for a whole range of k_{low} and k_{high} values. Fig. 4.4 shows how this parameter scan is completed for the $m = 4$ case as defined in Eq. 4.1. After choosing the parameters, a spectrometer using the filtered images is created and the full width at half prominence (FWHP) of the correlation curves are calculated, shown in Fig. 4.4(a). The calculation of correlation curves is explained later. Similarly, the reconstruction error for the spectrometer is calculated as the root mean square error (RMSE), shown in Fig. 4.4(b). After obtaining the array of RMSE, the set of parameters that lead to the smallest reconstruction error can be found, as indicated by the red cross in Fig. 4.4(a,b), the band-pass filter shape for this point is shown in Fig. 4.4(c). An example of a filtered speckle pattern can also be seen in Fig. 4.4(d) for a specific wavelength. In (a,b), the x axis is the higher cut-off (spatial) frequency, k_{high}, and the y axis is the lower cut-off (spatial) frequency, k_{low}. Since $k_{\text{high}} \geq k_{\text{low}}$, these scan arrays are triangular. Each axis is normalized by $2\pi/a$ where a is the core radius of the fiber. As an example, $k = 20$ corresponds to signals with a period of $a/20$. The filter shape shown in (c) has $|k_{\text{low}}| = 13.125(\text{x}2\pi/a)$ and $|k_{\text{high}}| = 17.5(\text{x}2\pi/a)$, which means the signals with period between $a/17.5$ and $a/13.125$ are left in the image. So, the speckle grains within this range of sizes are in the filtered image as shown in (d).

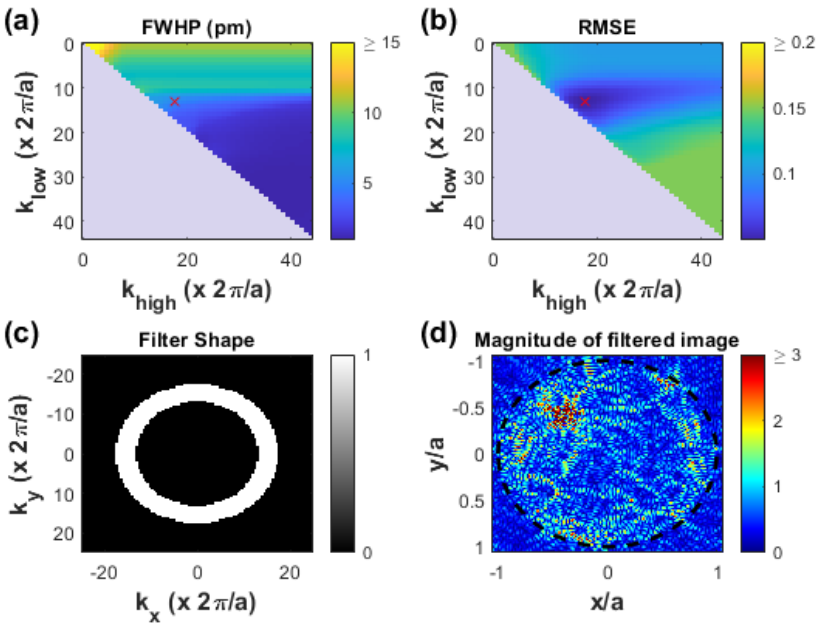

Figure 4.4: Figure showing the parameter scan for the cut-off values of the band-pass filter. **(a)** The FWHP of the correlation curve after filtering with the given cut-off values. **(b)** The RMSE of the reconstructed spectra using the filtered images with the given cut-off's. In (a,b), the x axis is the higher cut-off (spatial) frequency, k_{high}, and the y axis is the lower cut-off (spatial) frequency, k_{low}. **(c)** The shape of the optimal filter that gives the minimum RMSE shown with a red 'x' in the scan figures. The x and y axis in graph are the wavevectors, k_x and k_y normalized by $2\pi/a$. The filter shape has a $k_{\text{low}} = 13.125(\text{x}2\pi/a)$ and $k_{\text{high}} = 17.5(\text{x}2\pi/a)$, which means the signals with period between $a/17.5$ and $a/13.125$ are left in the image. **(d)** The amplitude of the filtered image for the optimal case at $\lambda = 1550$nm. The speckle grain sizes in this image should be between $a/17.5$ and $a/13.125$.

The speckle patterns decorrelate as the incoming wavelength is changed. For the original spectrometer, the decorrelation is measured to be around 8pm for a MMF described in the experimental setup [9]. In this study, we use filtered images instead of the raw speckle patterns to increase the resolution. Since the filtered images are complex, the inner product is calculated between the filtered images obtained at different wavelengths and then averaged over λ similar to the correlation definition in [9]. Inner product is the same as Pearson correlation as long as the images are real, as in the case of the raw images. This calculation can be written as

$$C_m(\Delta\lambda) = \left\langle I_m^{\text{filtered}}(\lambda + \Delta\lambda; x, y) \cdot I_m^{\text{filtered}}(\lambda; x, y) \right\rangle_\lambda \tag{4.4}$$

where, $A \cdot B$ denotes the inner product between A and B, and $\langle \ldots \rangle_\lambda$ is an average over λ. Fig. 4.5 shows the inner product for the original non-filtered and filtered images with different m. The inset plots the full-width-at-half-prominence (FWHP), $\delta\lambda$, which quantifies the spectral resolution of the system. The results show that for higher m values, lower FWHP values are obtained which is an enhancement in the resolution. For the purpose of the inset plot, the original spectrometer FWHP value is visualized at $m = 0$ since only $m \geq 1$ correspond to new results.

In order to test the spectrometer, an unknown spectrum needs to be reconstructed. The reconstruction algorithm as developed in [9], requires the measurement of a calibration data. This calibration data consists of the speckle pattern images for monochrome inputs scanning the whole bandwidth. Each speckle image is reshaped as a vector, then these vectors are used to construct the spectral reconstruction matrix as in [9]. The pseudo-inverse of this can be used for unknown speckle images. Let the speckle image measured at λ be represented as $I(x, y, \lambda)$ with N_{pixel} number of pixels in the image. The 2D image is reshaped into a vector as $I(r, \lambda)$ of size N_{pixel}x1. After this procedure, each vector is added as a column into a reconstruction matrix M. If the number of different wavelengths measured is N_λ the size of the matrix, M, would be N_{pixel}xN_λ. Let $I_{\text{unknown}}(x, y)$ be an image whose spectrum is unknown. In order to reconstruct the spectrum for this image, after reshaping it to, $I_{\text{unknown}}(r)$, a vector of size N_{pixel}x1, it is multiplied by the inverse matrix M^{-1} as

$$S_{\text{unknown}}(\lambda) = M^{-1} \cdot I_{\text{unknown}}(r) \tag{4.5}$$

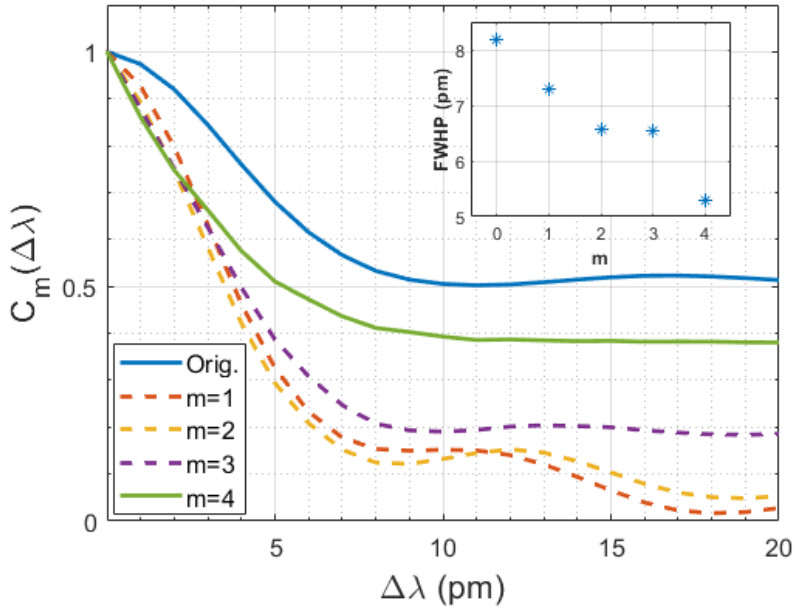

Figure 4.5: Correlation versus wavelength variation. As the wavelength is changed, the speckle patterns differentiate and the similarity decreases. For larger m, the filtered images result in steeper decorrelation which corresponds to a better spectral resolution overall. **(Inset)** FWHP versus m. The negative slope shows that the filtered images have better resolution.

where the size of M^{-1} is N_λxN_{pixel} and thus the size of the reconstructed spectrum vector, $S_{\text{unknown}}(\lambda)$, is N_λx1. The values in the spectrum vector $S_{\text{unknown}}(\lambda)$ tells the fraction of energy at each wavelength λ. As long as, the columns of M are orthogonal to each other, successful reconstruction should be possible. The columns would be orthogonal to each other if the inner product is small. Since the inner product for real valued images is proportional to the Pearson correlation, orthogonality can be evaluated using Pearson correlation.

Fig. 4.6(a) illustrates the reconstruction of a number of different spectra. Monochrome inputs within the whole range of bandwidth can be reconstructed accurately. An input spectrum which has two peaks separated by only 4 pm can be distinguished as shown in Fig. 4.6(b). We know from the FWHP value that the spectral resolution is around 5 pm which is sufficient to reconstruct two peaks that are separated by only 4 pm.

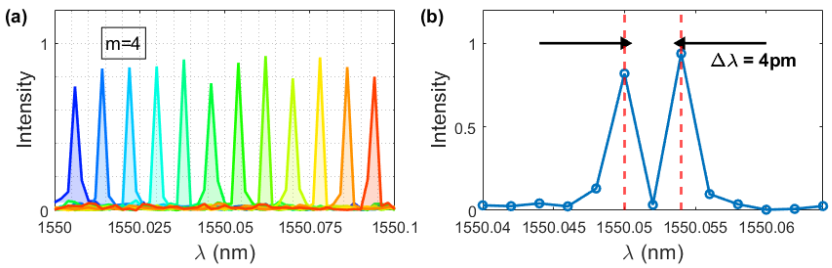

Figure 4.6: Spectral reconstruction for the minimum RMSE of 0.05 which has a resolution of around 5 pm. **(a)** 12 different reconstructed spectra for monochrome inputs that are equally spaced within the bandwidth shown. **(b)** Spectral reconstruction of an input which has two monochrome beams separated by only 4 pm. Two peaks are clearly distinguishable indicating that the 5 pm de-correlation width is sufficient to reconstruct spectrum with 2 pm steps as in the figure.

The chosen point on the parameter space in Fig. 4.4 is not the only choice that could be made. If another point with a smaller FWHP but a higher RMSE was chosen, the results would have been different. Fig. 4.7 shows the reconstruction for such a point with $k_{\text{low}} = 18.375(\text{x}2\pi/a)$ and $k_{\text{high}} = 23.625(\text{x}2\pi/a)$. The peaks are distinguishable since the FWHP is 2 pm however the peak values are less than 1 showing that the reconstruction is worse as expected from the high error of RMSE $= 0.10$. However, the calculated spectral resolution is better as it is seen in Table 4.2.

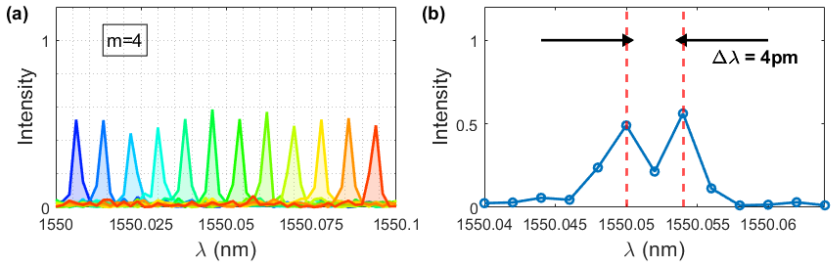

Figure 4.7: Spectral reconstruction for a different point with 1.8 pm FWHP and RMSE around 0.11 which is higher than minimum. **(a)** 12 different reconstructed spectra for monochrome inputs that are equally spaced within the bandwidth shown. **(b)** Spectral reconstruction of an input which has two monochrome beams separated by only 4 pm. Two peaks are clearly distinguishable however the y value is not 1 which is why the reconstruction is not optimal.

Table 4.2: Spatial filtering with different cut-off frequencies.

Filter Choice	$k_{\text{low}}(\text{x}2\pi/a)$	$k_{\text{high}}(\text{x}2\pi/a)$	FWHP	RMSE (au)
Fig. 4.6	13.125	17.5	5 pm	0.05
Fig. 4.7	19.25	23.625	1.8 pm	0.11

In this study, we report a technique which we call "structured illumination spectroscopy", because of the control on the input wavefronts applied to MMF spectrometer. The wavefront control employed here does not require any complicated procedure such as phase conjugation, speckle optimization, machine learning, or transmission matrix measurement. It is sufficient to measure the intensity speckle patterns for a few phase modulations which can be created using a Hadamard matrix within milliseconds. The speckle patterns are spatially filtered to create an image that is more sensitive to variations in the spectrum. The modulated speckle patterns can be considered as uncorrelated images where each modulation introduces different wavelength dependencies.

The spectral resolution with the smallest reconstruction error reported in this study is around 5pm while the original spectrometer without WFS or spatial filtering was 8pm [9] for the same MMF. A record resolution of 1.5pm has been reported previously

using 100m MMF [10]. If the same MMF was used here, a record of sub-picometer spectral resolution would be expected since the resolution increases linearly with the fiber length [9]. The wavelength selectable laser used in this study has a minimum 1pm step-size which prevents the measurement of sub-picometer spectral resolutions.

Even though this technique is applied on MMF spectrometers here, it can be applied in spectrometers based on a photonic chip [11] where an enhancement in spectral resolution could be much more difficult to achieve. Furthermore, the results of this study raises questions on what WFS can achieve in multimode systems. Utilizing WFS to manipulate the spectral activity can be crucial in various other studies. In general, spatial WFS can play a significant role where the spatial and spectral dynamics are coupled, and this study provides a solid output in this direction.

4.1.2 Activation Function

The second method developed for post-processing involves the activation function which will be explained in this section. This processing is implemented after recording the speckle patterns for a number of different SLM patterns at all wavelengths of interest. This process is visualized in Fig. 4.8(c). The speckles obtained for different vectors are subtracted from each other and passed through a ramp function (alternatively, a rectified linear unit) which is the activation function. Hence, after the subtraction, if the value of a pixel is negative, it is set to zero. An example of the resulting images for a single wavelength are shown in Fig. 4.8(d). As more speckles are subtracted, more pixels in the processed images become zero. This processing step can be thought of as extracting the intensities that are unique to the speckles obtained from only one Hadamard vector.

To express the technique analytically, let $I_n^{raw}(\lambda; x, y)$ be the raw output speckle pattern without any processing obtained for the n^{th} Hadamard vector at λ. The processed image can be expressed as

$$I_m^{processed}(\lambda; x, y) = max\left(0, I_1^{raw}(\lambda; x, y) - \sum_{k=2}^{m} I_k^{raw}(\lambda; x, y)\right) \tag{4.6}$$

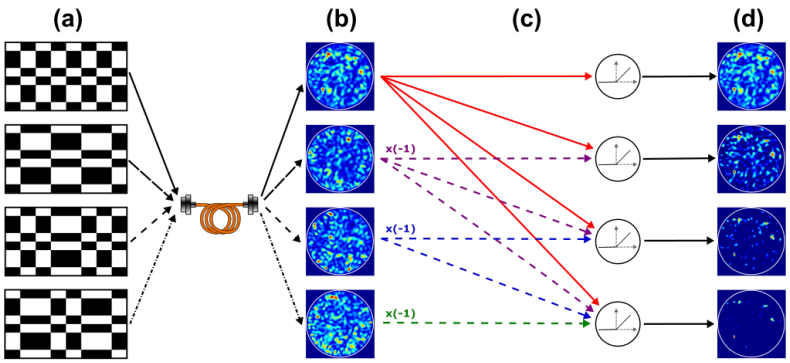

Figure 4.8: An illustration of the processing method. **(a)** The patterns displayed on the SLM for phase modulation. Each pattern is created using a vector drawn from the Hadamard matrix. The black regions represent 0 phase modulation while white regions represent π modulation. **(b)** The speckle patterns obtained at a single wavelength for the corresponding SLM patterns. **(c)** The obtained images are subtracted from each other. Afterwards, the total image is passed through a ramp function. **(d)** The final output images at a single wavelength for different m values.

where, m is a positive integer while $m = 1$ can be simplified to $I_1^{processed} = I_1^{raw}$, which is what the ordinary speckle spectrometers use [1]. As m increases, eventually, all pixels will become zero in the processed image and no information will be left. However, there is a convenient range of m values where this operation will extract unique information from various wavefront-shaped speckle patterns that provide an additional frequency dependence for increasing resolution.

The non-processed, raw speckle patterns decorrelate as the incoming wavelength is changed as shown in Fig. 4.9 with $m = 1$. The decorrelation is measured to be around 8pm for a MMF described in the experimental setup. Since the processed image for $m = 1$ is exactly equal to the raw speckle pattern, we observe the same resolution reported in [9].

The spectral dependence for raw and processed speckle patterns can be evaluated using Pearson correlation which is calculated between the images obtained at different wavelengths and then averaged over λ. This calculation can be described as

$$C_m(\Delta\lambda) = \left\langle r\left(I_m^{\text{processed}}(\lambda+\Delta\lambda; x, y), I_m^{\text{processed}}(\lambda; x, y)\right)\right\rangle_\lambda \tag{4.7}$$

where, $r(A, B)$ denotes the Pearson correlation between A and B, and $\langle \ldots \rangle_\lambda$ is an average over λ. Fig. 4.9(a) shows $C_m(\Delta\lambda)$ with different m. The full-width-at-half-prominence (FWHP) denoted by $\delta\lambda$ of the curves in 4.9(a) is plotted in Fig. 4.9(b). The results show that for higher m values, lower FWHP values and hence higher resolutions are obtained.

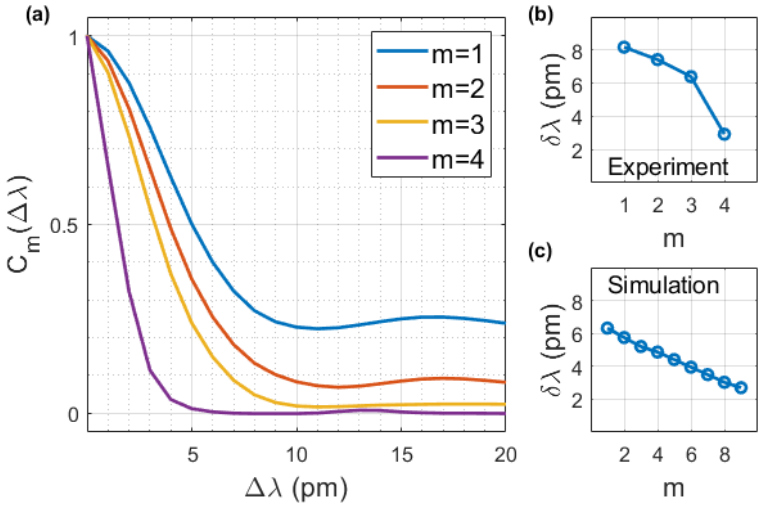

Figure 4.9: **(a)** Correlation curve as the wavelength is varied for different m. **(b)** The FWHP of correlation curves vs m. **(c)** The FWHP of correlation curves vs m in a simulation environment.

The developed technique has also been verified in a numerical MMF simulation and the FWHP results are shown in 4.9(c). The simulation is carried out using the MATLAB which developed in the earlier chapters. Here, each element of the mode-to-mode TM is taken as a normal random variable and the amplitude of the incoming beam has a 2D Gaussian shape. The wavelength dependent calculations include the assumptions made earlier that the bandwidth is much smaller than the central wavelength. Experimental and simulation plots agree that further processing (higher m values) decrease the FWHP. The small difference between the simulation and experiment results can be neglected considering the assumptions in modeling the simulation and the environmental conditions in the experiment. Nevertheless, both curves have a decreasing trend which shows the advantage of utilizing WFS and the proposed processing algorithm for spectrometer design.

While the codes developed in earlier sections are used in the simulation, this is an appropriate point to illustrate all the steps altogether in Fig. 4.10. This figure shows two example LP mode amplitudes (a,b), the amplitude of the TM (c), the amplitude (d,e,f) and phase (g,h,i) of the input field right before the MMF (d,g), the field right after coupling into the MMF (e,h) and the output field right after the MMF (f,i), and the processed speckle images for $2 \leq m \leq 4$ (j,k,l).

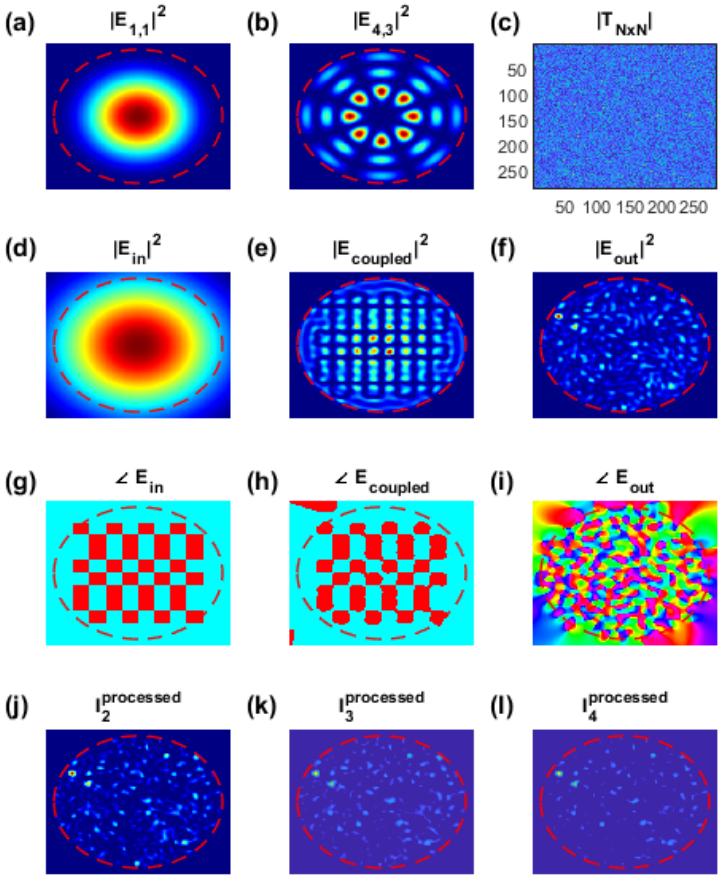

Figure 4.10: Simulation results are shown in the figure. **(a,b)** Two example LP mode amplitudes. **(c)** The amplitude of the TM. The intensity **(d)** and phase **(g)** of the input field right before the MMF. The intensity **(e)** and phase **(h)** of the field right after coupling into the MMF. The intensity **(f)** and phase **(i)** the output field after the MMF. **(j,k,l)** The processed images for $2 \leq m \leq 4$.

The procedure described in Eq. 4.6 can be generalized by introducing a new threshold

parameter, I_{Th}, as

$$I_m^{\text{processed}}(\lambda; x, y) = \max\left(I_{Th}\ ,\ \ I_1^{\text{raw}}(\lambda; x, y) - \sum_{k=2}^{m} I_k^{\text{raw}}(\lambda; x, y)\right) \tag{4.8}$$

The specific case $I_{Th} = 0$ is equivalent to Eq. 4.6. The FWHP for different I_{Th} is plotted in Fig. 4.11(a) up to $m \leq 5$. At $I_{Th} = 0$, $m = 5$ cannot be seen because for this value of I_{Th}, there are speckle patterns with all pixel values equal to I_{Th}. This situation hinders the correlation measurement as well as spectral reconstruction. Hence, for each m value, there is a range of I_{Th} which causes an enhanced resolution as well as a range that has a feasible spectral reconstruction.

Fig. 4.11 shows the FWHP (a) and mean-squared error (b) for spectrometers constructed using different threshold values. The spectra of a number of monochromatic speckle patterns within the bandwidth are reconstructed, and the average mean-squared error is plotted in this graph. The $m = 4$ case at $I_{Th} = 0$ seems to have both a high resolution and a low reconstruction error which makes it a good spectrometer.

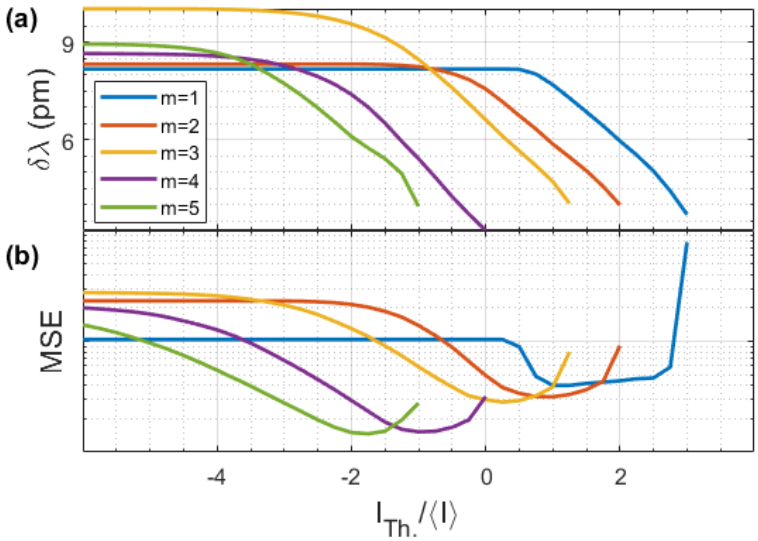

Figure 4.11: The FWHP **(a)** and MSE **(b)** of the spectrometer vs the threshold value.

The reconstruction method outlined in [9] is implemented here on the processed images instead of the raw speckle patterns. Although in [9], only a fraction of all the pixels are used during reconstruction, all pixels are used in this study because the processed images have less non-zero pixels. If the chosen pixels were all zero, by co-

incidence, around a certain wavelength, reconstruction would fail around that wavelength. This is observed for sufficiently high I_{Th} values for all m values.

Fig. 4.12 shows the reconstructions for different spectra with different processed images. A step size of 1 pm is used for all cases. Fig. 4.12(a,c) show the reconstructed spectra for different monochromatic inputs for the original case, $m = 1$, and for the $m = 4$ case, respectively. The difference is small but the $m = 4$ case has narrower peaks than the original $m = 1$ case which is an indication of the resolution enhancement. Fig. 4.12(b,d) show the reconstruction for a spectrum that has two monochromatic lights separated by only $\Delta\lambda = 3$pm for the original case, $m = 1$, and for the $m = 4$ case, respectively. The $m = 4$ case, unfortunately, cannot distinguish these two peaks. The reason for this is the non-linearity of the processing used in this section which is caused by the ramp function in the processing step.

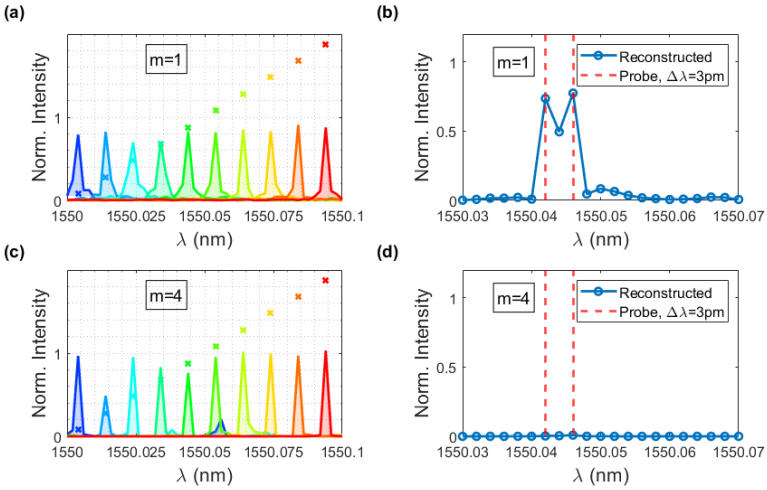

Figure 4.12: Reconstructed monochrome spectra **(a,c)** and reconstructed double-peak spectrum **(b,d)** for the original **(a,b)** and processed **(c,d)** spectrometers.

Since the spectrometer constructed in this section can reconstruct monochrome inputs but cannot reconstruct arbitrary spectra, this is a wavelength-meter rather than a spectrometer. Since this is only a wavelength-meter, the input speckle image can be normalized before applying any algorithm on it. This normalization will allow the spectral monochrome peak to be around 1 whatever the incoming laser power is. The enhancement in the spectral resolution is still valid for this wavelength-meter which is around 3 pm.

In Fig. 4.12, threshold values resulting in minimum MSE are chosen. Alternatively, threshold values resulting in minimum FWHP could have been chosen. Fig. 4.13 shows the reconstruction for both situations for $1 \leq m \leq 4$. The spectra in (b1-4) are for low FWHP, high MSE however the pre-normalization on the speckle image ensures all peaks are near 1. For this wavelength-meter, even though the MSE is high is some cases, the monochrome spectrum can be reconstructed thanks to the normalization. The FWHP and MSE values for all cases are summarized in Table 4.3.

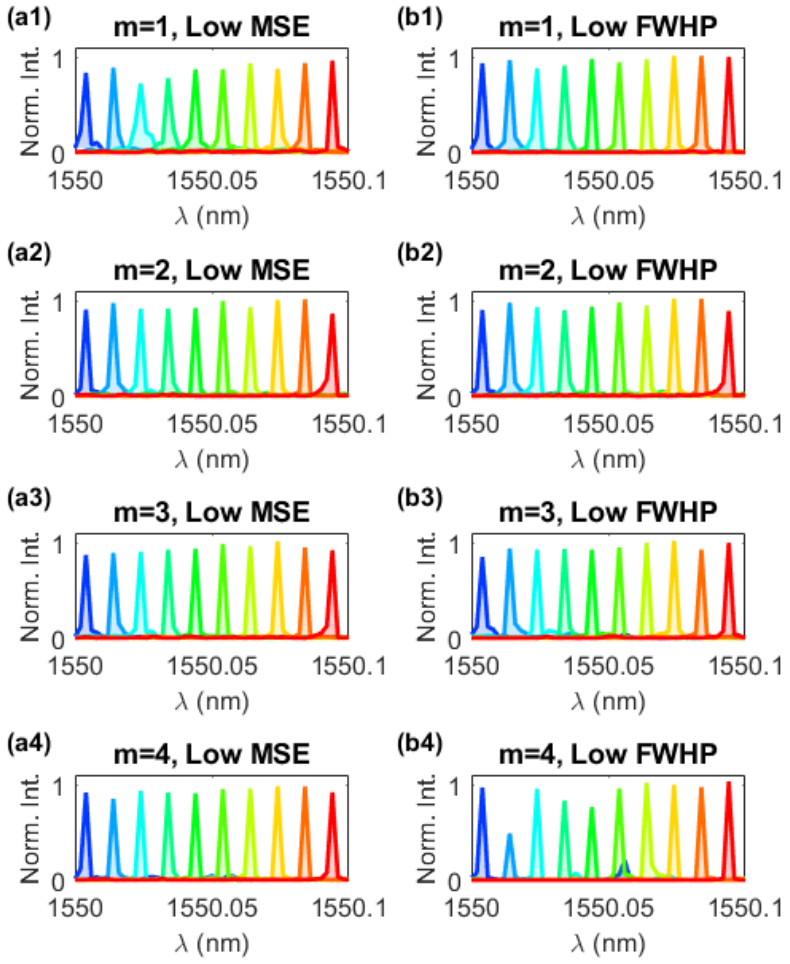

Figure 4.13: Reconstructed monochrome spectra for $1 \leq m \leq 4$ for low RMSE **(a1-4)** and for low FWHP **(b1-4)**.

Table 4.3: Activation function processing with different thresholds.

m	Choice	$I_{\text{Th}}/\langle I \rangle$	FWHP	MSE (au)
1	Low MSE	1	7.7 pm	0.040
2	Low MSE	1	5.9 pm	0.032
3	Low MSE	0.25	6.1 pm	0.028
4	Low MSE	-1	5.4 pm	0.015
1	Low FWHP	3	3.7 pm	0.781
2	Low FWHP	2	4.0 pm	0.091
3	Low FWHP	1.25	4.0 pm	0.080
4	Low FWHP	0	3.2 pm	0.032

4.2 Mode Filtering

The previous section highlights how speckle pattern processing can enhance the spectral resolution. In order to further understand the underlying physics, the LP modes and their wavevector values β_{mp} should be considered. Each LP mode field alternates as the wavelength is varied. In simulations, certain assumptions also valid in the experiments, lead to Eq. 2.19 which shows how the phase of an LP mode depends on the wavelength. Each LP mode should obtain a phase of

$$\phi_{mp} = \beta_{mp} L = \frac{2\pi}{\lambda} b_{mp} L \tag{4.9}$$

where $n_{clad} < b_{mp} < n_{core}$ is the normalized wavevector and L is the fiber length. An analysis in [9] considers only the maximum and minimum β_{mp} values, β_{max} and β_{min}, for an approximation of the expected resolution. This gives the relationship between

resolution and fiber parameters such as the length, NA etc. Although it is unimportant for their results due to the proportionality, the analysis ignores the effect of LP modes with intermediate β_{mp} values. It might be possible to create an energy distribution between the LP modes and enhance the spectral resolution with a trade-off on the bandwidth. For example, if only two LP modes with β_{max} and β_{min} carry energy while the other modes do not, the resolution would be better than the situation where all LP modes carry the same amount of energy. Of course, if only two modes are excited, the bandwidth would be considerably smaller because the speckle intensity would simply alternate between the same patterns. Nevertheless, it is meaningful to use the underlying fiber physics to cleverly choose the excited LP modes and enhance the resolution.

Therefore, in this section, LP mode distributions are used to "mode filter" the speckle patterns before constructing the spectrometer. To obtain the coefficients, c_{mp}, the speckle pattern should be measured as a complex field. For this purpose, the phase conjugation setup in Fig. 3.14 is used. Also, the input is chosen to be the lowest LP mode of $(0, 1)$ and sent into the fiber using amplitude and phase modulation. (It could have been wiser to send other input field distributions but that should also be chosen cleverly.) An example of a speckle pattern whose amplitude and phase are measured is shown in Fig. 4.14(a,b). The LP mode coefficients within this speckle pattern are calculated by taking the inner product with the given LP mode field. Afterwards, the total field is re-constructed using the coefficients and the mode field distributions. The field reconstructed using the LP modes is also shown in Fig. 4.14(c,d). The intensity distributions are clearly very similar which is an indication that the speckle pattern is in fact a linear summation of the LP modes used here.

The information of LP mode excitation levels could be useful in understanding the system further. First, Fig. 4.15(a) shows the mode coefficient amplitudes averaged over all the measured wavelengths. The wavevector values are normalized by β_{mp}/k_0 where $k_0 = 2\pi/\lambda$. Clearly, there is a trend in depending on β_{mp}. Lower (m, p) modes (that is higher β_{mp}), have higher coefficients which is an indication that these modes are easier to couple into. Fig. 4.15(b,c) show the amplitude and phase of the coefficients of three different modes over the wavelength range.

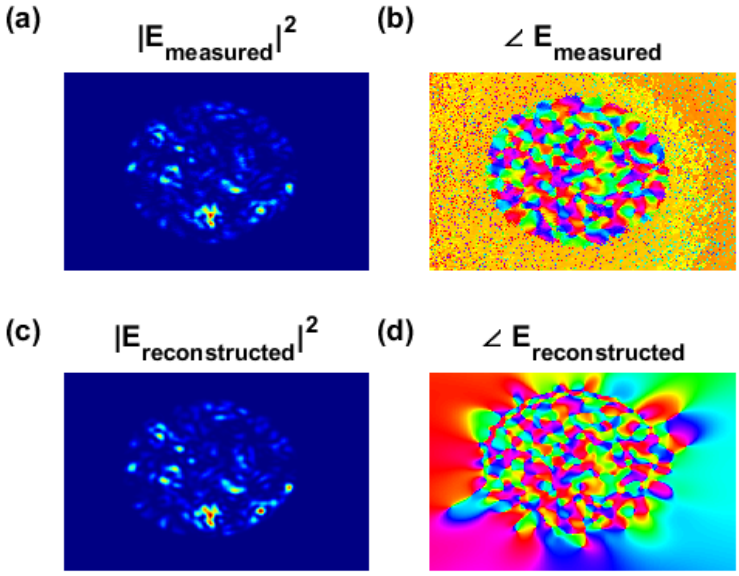

Figure 4.14: Complex field intensity **(a)** and phase **(b)** of a typical speckle pattern. Complex field intensity **(c)** and phase **(d)** of the same field reconstructed using LP modes.

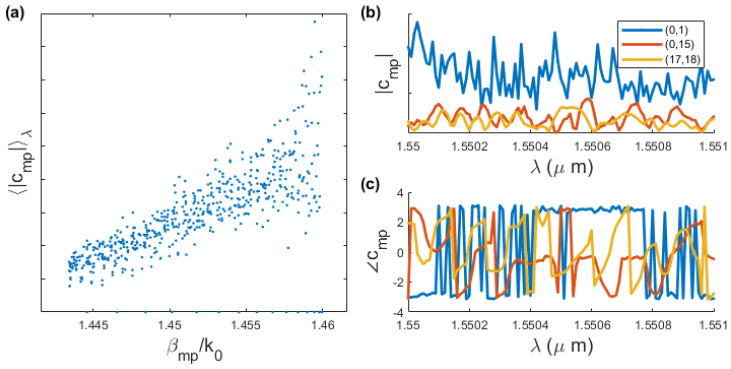

Figure 4.15: **(a)** LP mode coefficient amplitudes averaged over the wavelength. Amplitude **(b)** and phase **(c)** of three different LP mode coefficients with respect to the wavelength.

These $c_{mp}(\lambda)$ plots are not very informative as they are, but the auto-correlation should be more meaningful. Fig. 4.16(a) shows the auto-correlation amplitude, $|R_{mp}(\Delta\lambda)|$, of three example LP mode coefficients. Fig. 4.16(b) is the auto-correlation amplitude of all the LP modes with respect to β_{mp}.

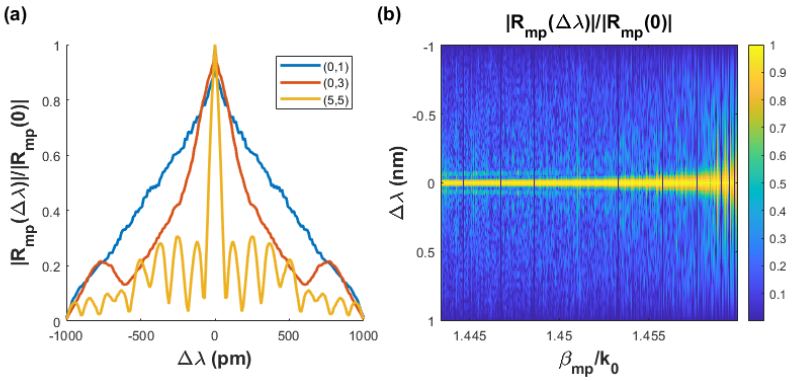

Figure 4.16: **(a)** Normalized auto-correlation amplitude of three LP mode coefficients. The x axis is the wavelength variation related to the auto-correlation measurement and the y axis is the normalized auto-correlation value. **(b)** Normalized auto-correlation amplitude of all LP mode coefficients with respect to wavevector values. The x axis is the wavevector value of the LP mode, y axis is the wavelength variation related to the auto-correlation measurement, and the color scale represents the normalized auto-correlation value.

The auto-correlation amplitude curves show how self similar the coefficients are with respect to the wavelength. The FWHP of these curves should be informative because these values will effectively determine the spectral resolution of the speckle spectrometer. Fig. 4.17 shows the FWHP of the auto-correlation amplitudes for each LP mode with respect to β_{mp}.

Clearly, there is a trend in the FWHP with respect to β_{mp}. This shows that the wavevector value has major impact on how self similar the coefficients they are which will affect the spectral resolution. If the LP modes with low β_{mp} values and thus lower FWHP values carry more energy within the speckle, the spectral resolution should be higher. Then, a band-pass or band-stop filter can be implemented with cut-off values of β_1 and β_2. In this technique with $\beta_1 < \beta_2$, the new filtered coefficients can be

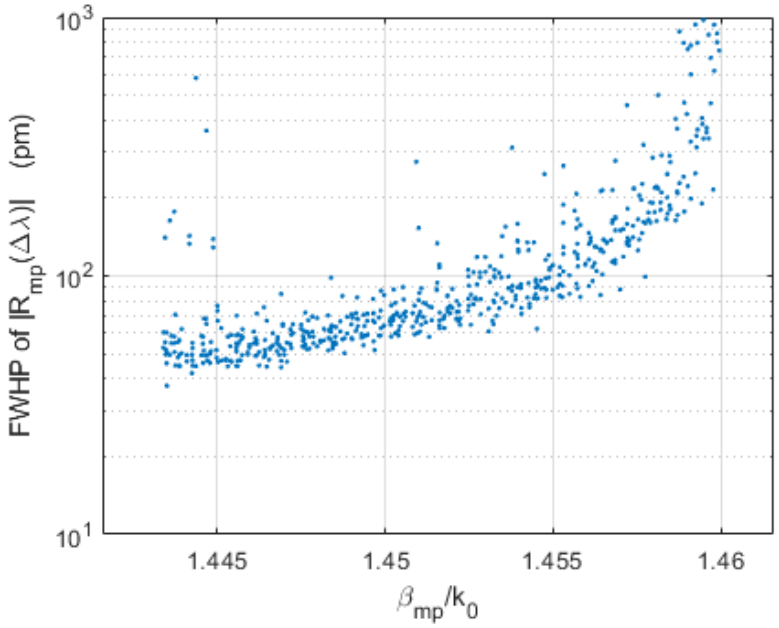

Figure 4.17: FWHP of the auto-correlation amplitudes of LP mode coefficients.

calculated as

$$c_{mp}^{\text{filtered}} = \begin{cases} c_{mp}, & \text{if } \beta_1 < \beta_{mp} < \beta_2 \\ 0, & \text{otherwise} \end{cases} \tag{4.10}$$

where c_{mp}^{filtered} is the final mode coefficient values used to reconstruct the complex speckle fields for the spectrometer. Similarly, if $\beta_2 < \beta_1$, a band-stop filter can be applied as

$$c_{mp}^{\text{filtered}} = \begin{cases} 0, & \text{if } \beta_2 < \beta_{mp} < \beta_1 \\ c_{mp}, & \text{otherwise} \end{cases} \tag{4.11}$$

This mode filtering technique is still linear because it can be represented by three consecutively applied matrices on the measured complex field. The first matrix of size N_{mode}xN_{pixel} calculates the mode coefficients. The second matrix of size N_{mode}xN_{mode} represents the chosen "mode filter". The third matrix of size N_{pixel}xN_{mode} converts the filtered coefficients to a 2D image. Therefore the whole procedure is linear and, as a consequence, arbitrary spectra can still be reconstructed.

Different "mode filters" are tried by scanning a range of β_1 and β_2 values. The FWHP and RMSE values for the corresponding spectrometer are shown in Fig. 4.18.

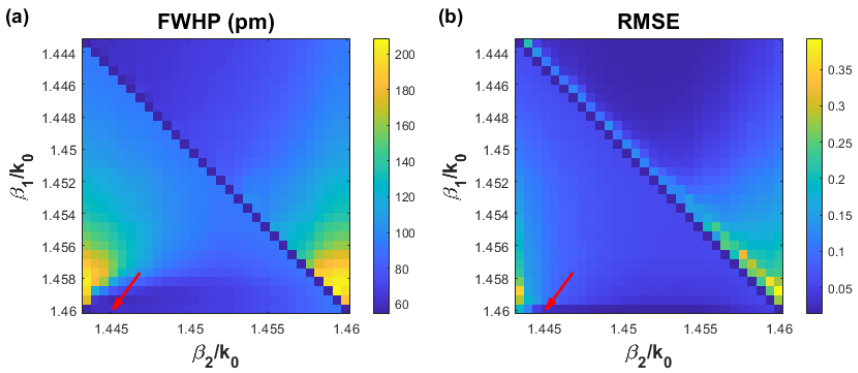

Figure 4.18: The FWHP **(a)** and RMSE **(b)** results obtained from different mode filters for different pairs of cut-off values.

It is important to choose a set of parameters that result in a low FWHP and RMSE. So, a plot showing both results, as shown in Fig. 4.19(a), can be useful. Each point on this plot corresponds to a different pair of cut-off values that was tried. A point shown with an arrow in the figure is qualitatively chosen because it has a low FWHP as well as a low RMSE. For the chosen point, the filtered mode excitation's are plotted in Fig. 4.19(b). It can be seen that the filter is basically a low-pass filter which makes sense when the auto-correlation FWHP values in Fig. 4.17 are considered. Even though a wider range of β_{mp} would result in a higher resolution, a low-pass filter seems to function with a higher resolution here. The reason for this could be experimental effects that are unaccounted for in that analysis. Since these modes, have many grains, are sensitive and harder to couple into, it is possible that experimental imperfections lead to a unexpected but welcome wavelength dependence. So, maybe the c_{mp} for these modes still effectively depend on the same $\beta_{\text{high}} = 2\pi n_{\text{core}}/\lambda$.

The corresponding spectrometer is constructed, and has a typical speckle pattern as shown in Fig. 4.20(a). In Fig. 4.20(b) is the correlation curve of the spectrometer which is calculated using the inner product of complex fields. The FWHP is calculated around $\delta\lambda = 61$pm which is better than the original value of around $\delta\lambda = 80$pm.

The spectrometer is also used to reconstruct different spectra. In Fig. 4.20(c) is the reconstructed spectra for various monochrome input beams. In Fig. 4.20(d) is the reconstructed spectrum of an input with monochrome peaks that are separated by only 40pm. The peaks can be distinguished since the spectral resolution is near this

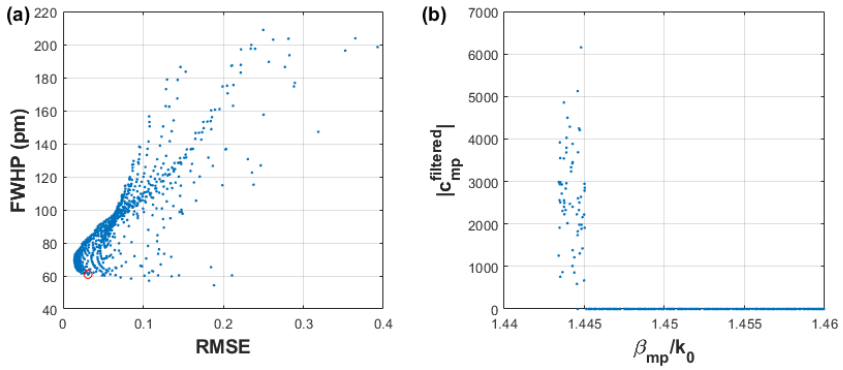

Figure 4.19: **(a)** RMSE vs FWHP of the spectrometers tried in the cut-off scan procedure. **(b)** Filtered mode coefficients at the indicated point.

value.

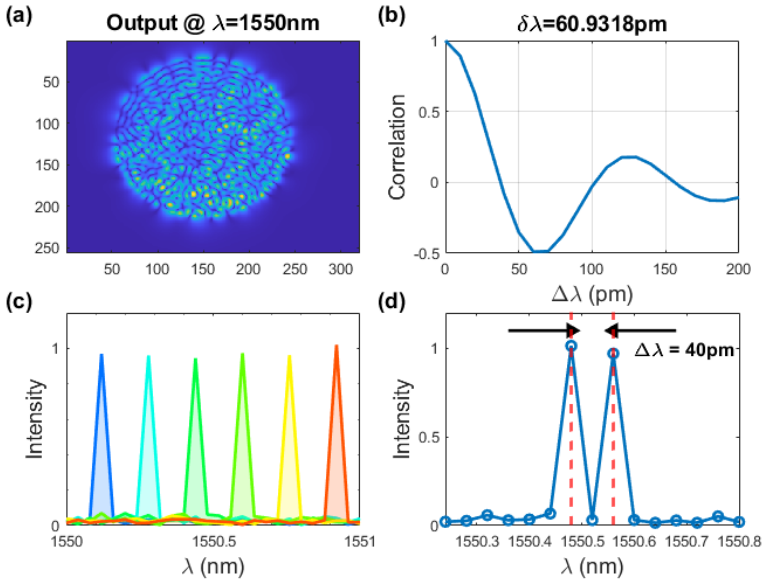

Figure 4.20: **(a)** Typical field amplitude after mode filtering. **(b)** Correlation curve after mode filtering. The FWHP of this curve is around 61pm. **(c)** Reconstructed monochrome spectra. **(d)** Reconstructed spectrum with two peaks separated by 40pm.

Additional to the selected parameters, it is possible to try other parameters that result in different FWHP and RMSE values. Table 4.4 summarizes the results for a few different cases. In fact, the third and fifth rows in the table in very similar mode filters even though the filter types are different. A similar situation is also valid for the second and fourth rows. Fig. 4.21 show the reconstructions for the second and third

rows. It can be seen in (a,b) that the spectra cannot reconstructed for this case of 54.3 pm resolution. (c,d) show the low RMSE case which has a reliable reconstruction. As a result, the intermediate choice, shown in Fig. 4.20, is a very good choice with low FWHP and RMSE.

Table 4.4: Mode filtering with different parameters.

Filter type	Choice	β_1/k_0	β_2/k_0	FWHP	RMSE (au)
Band-stop	Intermediate	1.4600	1.4451	60.9 pm	0.031
Band-stop	Low FWHP	1.4600	1.4434	54.3 pm	0.189
Band-stop	Low RMSE	1.4600	1.4525	69.4 pm	0.014
Band-pass	Low FWHP	1.4440	1.4445	59.7 pm	0.136
Band-pass	Low RMSE	1.4434	1.4525	69.4 pm	0.014

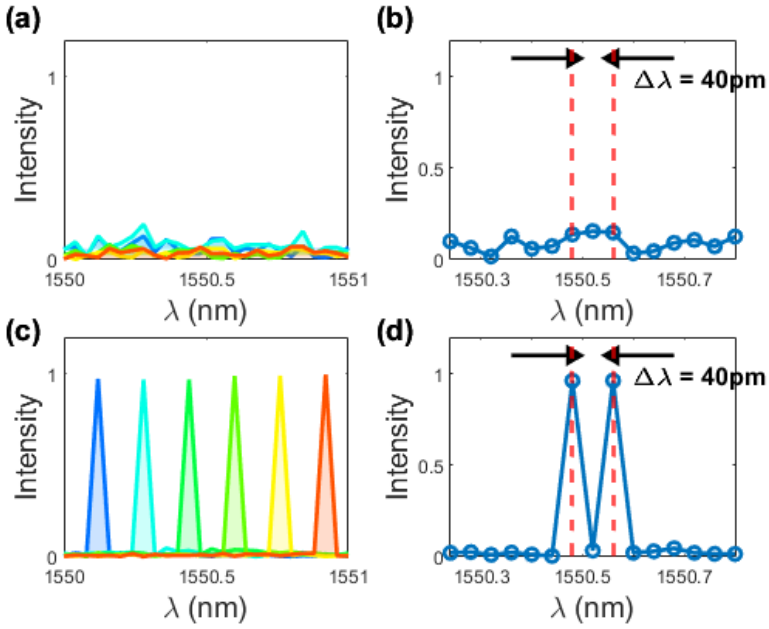

Figure 4.21: **(a)** Reconstructed monochrome spectra for the second row in Table 4.4. **(b)** Reconstructed spectrum with two peaks separated by 40pm for the second row in Table 4.4. **(c)** Reconstructed monochrome spectra for the third row in Table 4.4. **(d)** Reconstructed spectrum with two peaks separated by 40pm for the third row in Table 4.4.

4.3 Discussion

In the previous sections, different processing techniques were applied on the output of the fiber. Even though the input beam was modulated, it was not chosen to couple directly into specific LP modes. The next step could be to send an input such that the laser directly couples into a set of desired LP modes instead of filtering the output field. Since this would only determine the input energy distribution, the output energy distribution would not be directly affected. In order to couple into a desired set of LP modes at the output of the MMF, it is necessary to measure the mode-to-mode TM of the MMF. After obtaining the TM, the mode energies could be chosen such that the spectral resolution is increased similar to the mode filtering technique.

Since the setups constructed here can modulate the amplitude and phase for the input and measure the complex field at the output, it is straightforward to try a TM measurement. This measurement was attempted with the 2 m long 557 mode fiber. The results were not successful because the output speckle pattern was not similar to the target speckle pattern even when the inverse TM was used to tolerate for the mode mixing. The same calculation has been attempted with another 2 m long fiber which only has 6 LP modes. However the results were unsuccessful again. Hence, the results are not added to this thesis.

The main reason why mode-to-mode TM measurement was not successful is because 2 m is too long. In the literature, complete mode-to-mode TM measurements are done with fibers that are only a few centimeters long [56]. The longest fibers used are usually a few tens of centimeters [58] and these are not mode-to-mode but pixel-to-pixel TM studies. As a result, it is not surprising that mode-to-mode TM measurements were not successful. Nevertheless, the experimental and numerical methods developed here might be sufficient to measure the TM of a much shorter MMF.

Although TM measurement was not successful, the techniques explained in this chapter are capable of constructing MMF spectrometers with enhanced resolution using WFS on the input beam and post-processing on the output speckle patterns.

CHAPTER 5

CONCLUSION

In this study, WFS based techniques are used to enhance the spectral resolution of MMF based spectrometers. Three separate methods are developed. One of the methods reduce the device into a wavelength-meter due to its non-linearity however the other two methods are linear and function as a spectrometer. All methods involve the measurement of multiple speckle patterns under different input beam modulations. One of the methods also require the measurement of the complex field at the output and the numerical calculation of the LP modes.

As a result, in this thesis, the theory of MMF based spectrometers is explained. Numerical calculations of LP modes and spectral analysis for MMF based spectrometers are implemented. Experimental data of the speckle patterns are acquired using different setups under various input wavefront modulations. The experimental data have been analyzed and processed using three different methods so that the spectral resolution of the spectrometer is enhanced without changing the fiber.

To conclude, the methods developed here can be used with the same fibers used in the literature to obtain record level sub-picometer spectral resolutions. Also, the idea developed here, is to utilize spatial WFS in order to modify the spectral behaviour of a spatial-spectral coupled optical system.

In addition, the spectrometer that we develop here can be used to spectrally resolve the emission from quantum sources. Moreover, the speckle patterns can be analyzed to spatially, spectrally characterize quantum sources that are especially fabricated on 2D surfaces.

REFERENCES

[1] F. L. Pedrotti, L. M. Pedrotti, and L. S. Pedrotti, *Introduction to Optics*. Cambridge University Press, dec 2017.

[2] H. Cao, "Perspective on speckle spectrometers," *Journal of Optics*, vol. 19, p. 060402, jun 2017.

[3] M. Mazilu, T. Vettenburg, A. Di Falco, and K. Dholakia, "Random super-prism wavelength meter," *Optics Letters*, vol. 39, p. 96, jan 2014.

[4] M. Chakrabarti, M. L. Jakobsen, and S. G. Hanson, "Speckle-based spectrometer," *Optics Letters*, vol. 40, p. 3264, jul 2015.

[5] T. Yang, X. L. Huang, H. P. Ho, C. Xu, Y. Y. Zhu, M. D. Yi, X. H. Zhou, X. A. Li, and W. Huang, "Compact Spectrometer Based on a Frosted Glass," *IEEE Photonics Technology Letters*, vol. 29, pp. 217–220, jan 2017.

[6] P. Wang and R. Menon, "Computational spectrometer based on a broadband diffractive optic," *Optics Express*, vol. 22, p. 14575, jun 2014.

[7] E. G. Rawson, J. W. Goodman, and R. E. Norton, "Frequency dependence of modal noise in multimode optical fibers," *Journal of the Optical Society of America*, vol. 70, p. 968, aug 1980.

[8] W. Freude, C. Fritzsche, G. Grau, and Lu Shan-da, "Speckle interferometry for spectral analysis of laser sources and multimode optical waveguides," *Journal of Lightwave Technology*, vol. 4, no. 1, pp. 64–72, 1986.

[9] B. Redding, S. M. Popoff, and H. Cao, "All-fiber spectrometer based on speckle pattern reconstruction," *Optics Express*, vol. 21, no. 5, p. 6584, 2013.

[10] B. Redding, M. Alam, M. Seifert, and H. Cao, "High-resolution and broadband all-fiber spectrometers," *Optica*, vol. 1, p. 175, sep 2014.

[11] B. Redding, S. F. Liew, R. Sarma, and H. Cao, "Compact spectrometer based on a disordered photonic chip," *Nature Photonics*, vol. 7, no. 9, pp. 746–751, 2013.

[12] B. Redding, S. Fatt Liew, Y. Bromberg, R. Sarma, and H. Cao, "Evanescently coupled multimode spiral spectrometer," *Optica*, vol. 3, no. 9, p. 956, 2016.

[13] N. Coluccelli, M. Cassinerio, B. Redding, H. Cao, P. Laporta, and G. Galzerano, "The optical frequency comb fibre spectrometer," *Nature Communications*, vol. 7, p. 12995, dec 2016.

[14] S. F. Liew, B. Redding, M. A. Choma, H. D. Tagare, and H. Cao, "Broadband multimode fiber spectrometer," *Optics Letters*, vol. 41, p. 2029, may 2016.

[15] N. H. Wan, F. Meng, T. Schroder, R. J. Shiue, E. H. Chen, and D. Englund, "High-resolution optical spectroscopy using multimode interference in a compact tapered fibre," *Nature Communications*, vol. 6, p. 7762, nov 2015.

[16] B. Redding, S. M. Popoff, Y. Bromberg, M. A. Choma, and H. Cao, "Noise analysis of spectrometers based on speckle pattern reconstruction," *Applied Optics*, vol. 53, p. 410, jan 2014.

[17] K. Okamoto, *Fundamentals of Optical Waveguides*. Elsevier, 2006.

[18] B. Moslehi, J. W. Goodman, and E. G. Rawson, "Bandwidth estimation for multimode optical fibers using the frequency correlation function of speckle patterns," *Applied Optics*, vol. 22, p. 995, apr 1983.

[19] J. W. Goodman, *Speckle Phenomena in Optics: Theory and Applications, Second Edition*. SPIE, jan 2020.

[20] H. Yu, J. Park, K. Lee, J. Yoon, K. Kim, S. Lee, and Y. Park, "Recent advances in wavefront shaping techniques for biomedical applications," *Current Applied Physics*, vol. 15, pp. 632–641, may 2015.

[21] I. M. Vellekoop, "Feedback-based wavefront shaping," *Optics Express*, vol. 23, p. 12189, may 2015.

[22] R. Horstmeyer, H. Ruan, and C. Yang, "Guidestar-assisted wavefront-shaping methods for focusing light into biological tissue," *Nature Photonics*, vol. 9, pp. 563–571, sep 2015.

[23] A. P. Mosk, A. Lagendijk, G. Lerosey, and M. Fink, "Controlling waves in space and time for imaging and focusing in complex media," *Nature Photonics*, vol. 6, no. 5, pp. 283–292, 2012.

[24] I. M. Vellekoop and A. P. Mosk, "Focusing coherent light through opaque strongly scattering media," *Optics Letters*, vol. 32, p. 2309, aug 2007.

[25] I. M. Vellekoop, E. G. van Putten, A. Lagendijk, and A. P. Mosk, "Demixing light paths inside disordered metamaterials," *Optics Express*, vol. 16, no. 1, p. 67, 2008.

[26] R. Di Leonardo and S. Bianchi, "Hologram transmission through multi-mode optical fibers," *Optics Express*, vol. 19, p. 247, jan 2011.

[27] O. Tzang, E. Niv, S. Singh, S. Labouesse, G. Myatt, and R. Piestun, "Wavefront shaping in complex media with a 350 kHz modulator via a 1D-to-2D transform," *Nature Photonics*, vol. 13, no. 11, pp. 788–793, 2019.

[28] I. M. Vellekoop and A. P. Mosk, "Universal Optimal Transmission of Light Through Disordered Materials," *Physical Review Letters*, vol. 101, p. 120601, sep 2008.

[29] T. Zhao, S. Ourselin, T. Vercauteren, and W. Xia, "Seeing through multimode fibers with real-valued intensity transmission matrices," *Optics Express*, vol. 28, p. 20978, jul 2020.

[30] S. Resisi, Y. Viernik, S. M. Popoff, and Y. Bromberg, "Wavefront shaping in multimode fibers by transmission matrix engineering," *APL Photonics*, vol. 5, p. 036103, mar 2020.

[31] A. Drémeau, A. Liutkus, D. Martina, O. Katz, C. Schülke, F. Krzakala, S. Gigan, and L. Daudet, "Reference-less measurement of the transmission matrix of a highly scattering material using a DMD and phase retrieval techniques," *Optics Express*, vol. 23, p. 11898, may 2015.

[32] A. Boniface, M. Mounaix, B. Blochet, R. Piestun, and S. Gigan, "Transmission-matrix-based point-spread-function engineering through a complex medium," *Optica*, vol. 4, p. 54, jan 2017.

[33] T. Čižmár and K. Dholakia, "Exploiting multimode waveguides for pure fibre-based imaging," *Nature Communications*, vol. 3, p. 1027, jan 2012.

[34] D. Loterie, S. Farahi, I. Papadopoulos, A. Goy, D. Psaltis, and C. Moser, "Digital confocal microscopy through a multimode fiber," *Optics Express*, vol. 23, p. 23845, sep 2015.

[35] S. M. Popoff, G. Lerosey, R. Carminati, M. Fink, A. C. Boccara, and S. Gigan, "Measuring the Transmission Matrix in Optics: An Approach to the Study and Control of Light Propagation in Disordered Media," *Physical Review Letters*, vol. 104, p. 100601, mar 2010.

[36] S. Popoff, G. Lerosey, M. Fink, A. C. Boccara, and S. Gigan, "Image transmission through an opaque material," *Nature Communications*, vol. 1, p. 81, dec 2010.

[37] Y. Choi, C. Yoon, M. Kim, T. D. Yang, C. Fang-Yen, R. R. Dasari, K. J. Lee, and W. Choi, "Scanner-Free and Wide-Field Endoscopic Imaging by Using a Single Multimode Optical Fiber," *Physical Review Letters*, vol. 109, p. 203901, nov 2012.

[38] P. Caramazza, O. Moran, R. Murray-Smith, and D. Faccio, "Transmission of natural scene images through a multimode fibre," *Nature Communications*, vol. 10, p. 2029, dec 2019.

[39] B. Rahmani, D. Loterie, G. Konstantinou, D. Psaltis, and C. Moser, "Multimode optical fiber transmission with a deep learning network," *Light: Science and Applications*, vol. 7, no. 1, pp. 2047–7538, 2018.

[40] E. Kakkava, B. Rahmani, N. Borhani, U. Teğin, D. Loterie, G. Konstantinou, C. Moser, and D. Psaltis, "Imaging through multimode fibers using deep learning: The effects of intensity versus holographic recording of the speckle pattern," *Optical Fiber Technology*, vol. 52, p. 101985, nov 2019.

[41] E. Kakkava, N. Borhani, B. Rahmani, U. Teğin, C. Moser, and D. Psaltis, "Deep Learning-Based Image Classification through a Multimode Fiber in the Presence of Wavelength Drift," *Applied Sciences*, vol. 10, p. 3816, may 2020.

[42] U. Teğin, B. Rahmani, E. Kakkava, N. Borhani, C. Moser, and D. Psaltis, "Controlling spatiotemporal nonlinearities in multimode fibers with deep neural networks," *APL Photonics*, vol. 5, p. 030804, mar 2020.

[43] N. Borhani, E. Kakkava, C. Moser, and D. Psaltis, "Learning to see through multimode fibers," *Optica*, vol. 5, p. 960, aug 2018.

[44] P. Wang and J. Di, "Deep learning-based object classification through multimode fiber via a CNN-architecture SpeckleNet," *Applied Optics*, vol. 57, p. 8258, oct 2018.

[45] U. Kürüm, P. R. Wiecha, R. French, and O. L. Muskens, "Deep learning enabled real time speckle recognition and hyperspectral imaging using a multimode fiber array," *Optics Express*, vol. 27, p. 20965, jul 2019.

[46] R. French, S. Gigan, and O. L. Muskens, "Snapshot fiber spectral imaging using speckle correlations and compressive sensing," *Optics Express*, vol. 26, p. 32302, nov 2018.

[47] J. Bosch, S. A. Goorden, and A. P. Mosk, "Frequency width of open channels in multiple scattering media," *Optics Express*, vol. 24, p. 26472, nov 2016.

[48] M. G. L. Gustafsson, "Surpassing the lateral resolution limit by a factor of two using structured illumination microscopy. SHORT COMMUNICATION," *Journal of Microscopy*, vol. 198, pp. 82–87, may 2000.

[49] T. Pertsch, "Fiber mode solver (Bessel's differential equation)." `https://www.iap.uni-jena.de/iapmedia/de/Lecture/Computational+Photonics1538258400/CPho18_Seminar06_Fiber_Mode_Solver.pdf`, August 2021.

[50] M. Hughes, "Fibre Mode Solver and Simulator." `https://www.mathworks.com/matlabcentral/fileexchange/77497-fibre-mode-solver-and-simulator`, August 2017.

[51] V. Bagnoud and J. D. Zuegel, "Independent phase and amplitude control of a laser beam by use of a single-phase-only spatial light modulator," *Optics Letters*, vol. 29, p. 295, feb 2004.

[52] E. G. Putten, I. M. Vellekoop, and A. P. Mosk, "Spatial amplitude and phase modulation using commercial twisted nematic LCDs," *Applied Optics*, vol. 47, no. 12, pp. 2076–2081, 2008.

[53] J. A. Davis, "Encoding complex diffractive optical elements onto a phase-only liquid-crystal spatial light modulator," *Optical Engineering*, vol. 40, p. 327, feb 2001.

[54] V. Arrizón, "Complex modulation with a twisted-nematic liquid-crystal spatial light modulator: double-pixel approach," *Optics Letters*, 2003.

[55] P. M. Birch, R. Young, D. Budgett, and C. Chatwin, "Two-pixel computer-generated hologram with a zero-twist nematic liquid-crystal spatial light modulator," *Optics Letters*, vol. 25, p. 1013, jul 2000.

[56] S. Rothe, H. Radner, N. Koukourakis, and J. W. Czarske, "Transmission Matrix Measurement of Multimode Optical Fibers by Mode-Selective Excitation Using One Spatial Light Modulator," *Applied Sciences*, vol. 9, p. 195, jan 2019.

[57] J. Goodman, "Introduction to Fourier Optics 3ed," 2005.

[58] P. Jákl, M. Šiler, J. Ježek, J. Trägårdh, P. Zemánek, and T. Čižmár, "Multimode fiber transmission matrix obtained with internal references," in *Adaptive Optics and Wavefront Control for Biological Systems V* (T. G. Bifano, S. Gigan, and N. Ji, eds.), vol. 1088610, p. 35, SPIE, feb 2019.

[59] R. Florentin, V. Kermene, A. Desfarges-Berthelemot, and A. Barthelemy, "Fast transmission matrix measurement of a multimode optical fiber with common path reference," *IEEE Photonics Journal*, vol. 10, no. 5, pp. 1–6, 2018.

[60] S. M. Popoff, G. Lerosey, M. Fink, A. C. Boccara, and S. Gigan, "Controlling light through optical disordered media: transmission matrix approach," *New Journal of Physics*, vol. 13, p. 123021, dec 2011.

[61] L. V. Amitonova and J. F. de Boer, "Compressive imaging through a multimode fiber," *Optics Letters*, vol. 43, p. 5427, nov 2018.